HAL
open science

Mechanical analysis of a natural example of onland gravity gliding: The role of river incision and deposition

G. Messager, R. Hassani, Bertrand Nivière

To cite this version:

G. Messager, R. Hassani, Bertrand Nivière. Mechanical analysis of a natural example of onland gravity gliding: The role of river incision and deposition. Journal of Geophysical Research: Earth Surface, 2014, 119 (7), pp.1581-1603. 10.1002/2013JF003062 . hal-01059297

HAL Id: hal-01059297

https://hal.science/hal-01059297v1

Submitted on 1 Nov 2021

HAL is a multi-disciplinary open access archive for the deposit and dissemination of scientific research documents, whether they are published or not. The documents may come from teaching and research institutions in France or abroad, or from public or private research centers.

L'archive ouverte pluridisciplinaire **HAL**, est destinée au dépôt et à la diffusion de documents scientifiques de niveau recherche, publiés ou non, émanant des établissements d'enseignement et de recherche français ou étrangers, des laboratoires publics ou privés.

Copyright

AGU PUBLICATIONS

JGR

Journal of Geophysical Research: Earth Surface

RESEARCH ARTICLE

10.1002/2013JF003062

Key Points:

- Mechanical analysis allows validating an example of onland gravity gliding
- Gravity gliding is simulated with river erosion and deposition down the slope
- Analytical analysis estimating the critical slope to initiate gravity gliding

Correspondence to:
G. Messager,
gmess@statoil.com

Citation:
Messager, G., R. Hassani, and B. Nivière (2014), Mechanical analysis of a natural example of onland gravity gliding: The role of river incision and deposition, *J. Geophys. Res. Earth Surf.*, *119*, 1581–1603, doi:10.1002/2013JF003062.

Received 12 DEC 2013
Accepted 11 JUN 2014
Accepted article online 16 JUN 2014
Published online 21 JUL 2014

Mechanical analysis of a natural example of onland gravity gliding: The role of river incision and deposition

Grégoire Messager[1,2,3], Riad Hassani[4], and Bertrand Nivière[1]

[1]Laboratoire des Fluides Complexes et de leurs Réservoirs, UMR 5150-CNRS-TOTAL, Université de Pau et des Pays de l'Adour, IPRA, Pau, France, [2]Group of Dynamic of the Lithosphere, Institute of Earth Sciences "Jaume Almera", CSIC, Lluís Solé i Sabarís s/n, Barcelona, Spain, [3]Now at Statoil ASA, EXP RDI CPR CP, Bergen, Norway, [4]Observatoire de la Côte d'Azur, Géoazur UMR 7329–Université Nice-Sophia Antipolis, Valbonne, France

Abstract Gravity gliding implies rigid translation of a body down a slope where displacements are parallel to a tilted detachment plane. Although large-scale gravity gliding is commonly observed offshore, under conditions of high fluid overpressure and abundant upslope sedimentary supply, its occurrence on land is debated. We investigate the mechanical feasibility of such a process as well as the role of fluvial incision and sedimentation down the slope in the initiation of the gliding. We use a two-dimensional (2-D) finite element model combined with a 2-D failure analysis approach. The numerical models simulate the deformation and provide quantitative estimates of the failure criteria at the head and toe of the overburden. Analytical solutions approximate the numerical results by taking into account the fluvial incision and sedimentation, the internal friction angle, and the thickness and length of the overburden. Our models are based on a field example in the Andean foothills of Argentina, where gravity gliding of a 1000 m thick section is suspected above a crustal-scale anticline. The incision and sedimentation reduce and strengthen, respectively, the downslope resistance to contractional failure. The critical slope at which the gliding is initiated is reduced by fluvial incision and increased by sedimentation. We show that tectonic uplift may lead to large-scale gravity gliding on land where the overburden thickness is less than 2000 m. Incision facilitates and localizes the frontal shortening. Incision greater than 1000 m may trigger gliding for overburden up to 4000 m thick, while sedimentation thicker than 1000 m inhibits gliding. These results show that thin-skinned onland gravity gliding could be common in tectonically active regions where incision is important.

1. Introduction

In the last decades, increasing exploration of passive continental margins by the oil industry has provided a large set of 2-D and 3-D seismic data which have improved our understanding of postsalt structures such as diapirs and tectonic rafts [e.g., *Burollet*, 1975]. Halokinetic structures have been widely observed along the passive margins of West Africa [e.g., *Evamy et al.*, 1978; *Duval et al.*, 1992; *Lundin*, 1992; *Damuth*, 1994; *Cohen and McClay*, 1996; *Mauduit and Brun*, 1998; *Cobbold et al.*, 2009], Brazil [e.g., *Cobbold and Szatmari*, 1991; *Demercian et al.*, 1993; *Mohriak et al.*, 1995; *Szatmari et al.*, 1996; *Cobbold et al.*, 2004], and in the North Sea [e.g., *Duval et al.*, 1992; *Lundin*, 1992; *Penge et al.*, 1993; *Bishop et al.*, 1995], the Mediterranean Sea [*Loncke et al.*, 2006; *Sellier et al.*, 2013], and the Gulf of Mexico [*Worral and Snelson*, 1989; *Wu et al.*, 1990; *Rowan et al.*, 2000]. Diapirs and rafts have been commonly interpreted as the result of gravity-driven processes where large slides of sediment move seaward, generating upslope extension and downslope contraction [e.g., *Schultz-Ela*, 2001]. Two different types of dynamic models are presently invoked to explain gravity-driven tectonics at passive margins: (i) gravity spreading driven only by differential sedimentary loading and (ii) gravity gliding primarily due to margin tilt that allows the semirigid translation of a body downslope. The displacements take place parallel to a buried seaward dipping detachment layer made of salt or overpressured sediments [*Cobbold and Szatmari*, 1991; *Mauduit et al.*, 1997a, 1997b].

Mechanical conditions conducive to gravity-driven slides have been studied through the application of analytical theories, as well as by analogue and numerical modeling [e.g., *Mandl and Crans*, 1981; *Mourgues and Cobbold*, 2006; *Gemmer et al.*, 2005; *Brun and Fort*, 2011]. In the case of pure gravity spreading, the continental sediment discharge creates a surficial slope, producing a seaward directed pressure gradient that drives downslope movement. Dominant gravity gliding requires the tilting of the basement, which can be

©2014. American Geophysical Union. All Rights Reserved.

triggered by the thermal subsidence of young passive margins or by tectonic activity due to rifting or margin uplift [e.g., *Duval et al*., 1992; *Penge et al*., 1993; *Bishop et al*., 1995] or basement fault activity [*Sellier et al*., 2013]. The thickness (T) of the decoupled cover must be small with respect to its length (L) ($T/L < 0.1$) [e.g., *Messager et al*., 2014]. In both gravity gliding and spreading, a high rate of sedimentation fosters the displacement [e.g., *Worral and Snelson*, 1989; *Cobbold and Szatmari*, 1991; *Mauduit et al*., 1997a; *Gemmer et al*., 2004, 2005], and the presence of fluids increases the solid and fluid pressure in the sediments, which in turn reduces the failure criterion [e.g., *Gemmer et al*., 2005; *Mourgues et al*., 2009, 2014].

Gravity collapses are now widely recognized on land, more particularly in the core of orogens. In the French Alps, normal faults have been interpreted as resulting from 150 km long radial sliding above Triassic evaporites in the Provençal Basin of Southeast France [*Rangin et al*., 2010] or from crustal flow of the internal zones of the orogen toward the Mediterranean margin [*Larroque et al*., 2009]. At a smaller scale, multiple detachment layers may allow the decoupling of the sedimentary cover of foreland basins, regardless of the regional stress regime. Examples of such thin-skinned slides involve lower volumes of sediments ($<$100 km^3) than at crustal scale and are often associated with catastrophic events such as heavy rains or earthquakes. The most famous examples were described in Tsergo Ri (Nepal) [*Ibetsberger*, 1996] or in Golbi-Altay (Mongolia) [*Philip and Ritz*, 1999]. Other examples illustrate the role of surface processes in such thin-skinned slides. *Schultz-Ela and Walsh* [2002] showed that the gravitational collapse in Canyonlands National Park produced sliding toward the "downslope free edge" formed by the canyon of the Colorado River (Utah) [*McGill and Stromquist*, 1979]. *Mège et al*. [2013] made similar observations in the western Ogaden in Ethiopia.

Considering that differential sedimentary loading is negligible in the inner domain of the orogens, it is uncertain if gravity spreading could mechanically occur on land. However, most of the onland examples have been interpreted as gravity spreading [*Philip and Ritz*, 1999; *Schultz-Ela and Walsh*, 2002; *Lacoste et al*., 2009; *Rangin et al*., 2010] and are often associated with fluid overpressure [*Lacoste et al*., 2009] or a nonindurated rock body [*Philip and Ritz*, 1999]. Dominant gravity gliding has been rarely observed on land. Recently, *Messager et al*. [2014] described coeval thin-skinned stretching and shortening above the crustal front flexure of the southern Andean fold belts, interpreting these structures as the potential downslope slide of a ~30 km long and 1000 m thick raft of indurated and undeformed sediments. However, *Messager et al*. [2014] show that stretching on top of the slope may also result from the stress developed by flexure as inferred from mechanical analysis [e.g., *Friedman et al*., 1976] and natural examples [e.g., *Emami et al*., 2010]. The occurrence of dominant gravity gliding on land is not intuitive. Compared to the offshore settings, the rheological and geometrical (higher T/L) configurations would mechanically strengthen the overburden to failure. In addition, few natural examples support the model on land.

In this study, we investigate the mechanisms that could lead to dominant gravity gliding on land. We assume that tectonic uplift generates sufficiently steep slopes to initiate such instabilities. In addition, high basement uplift rates disturb mass transfers at the surface, leading to the deposition of large sediment volumes for periods of thousands to millions of years upstream of the uplifted area and to incision downstream due to regressive erosion or to river deflections [e.g., *Suppe et al*., 1992; *Jackson et al*., 1996; *Einsele and Hinderer*, 1997; *Horton and DeCelles*, 1997; *Humphrey and Konrad*, 2000; *Sobel et al*., 2003; *Garcia-Castellanos*, 2006]. Such sedimentation and incision could alter the downslope resistance to contractional failure, and thus interact with the critical conditions required for the initiation and maintenance of gravity gliding [*Schultz-Ela and Walsh*, 2002; *Lacoste et al*., 2011].

We argue that this process may occur in the Central Andes where Tertiary to Present inversion of Mesozoic rift basins has led to the segmentation of the foreland into broad crustal uplifted blocks and temporary intramountain basins [e.g., *Giambiagi et al*., 2001; *Hilley and Strecker*, 2005; *Messager et al*., 2010] and where tensional strain is encountered at the outer hinge of the uplifted blocks [*Ramos*, 1981; *Narciso et al*., 2000; *Galland et al*., 2007; *Folguera et al*., 2008; *Messager et al*., 2014]. We test here the onland gravity gliding model described by *Messager et al*. [2014]. We use the two-dimensional (2-D) finite element code ADELI associated with the dynamic relaxation method and realistic constitutive models [*Hassani et al*., 1997] to estimate the critical slope required for failure at the top and toe of a frictional-plastic sedimentary cover (*model 1*). We then test the influence of incision (*model 2*) and sedimentation (*model 3*) downslope of the uplifted area. Based on these results, we propose a 2-D analytical failure approach to assess realistic configurations under which gravity gliding could occur on land. This approach yields an approximation of the numerical result that takes into

©2014. American Geophysical Union. All Rights Reserved.

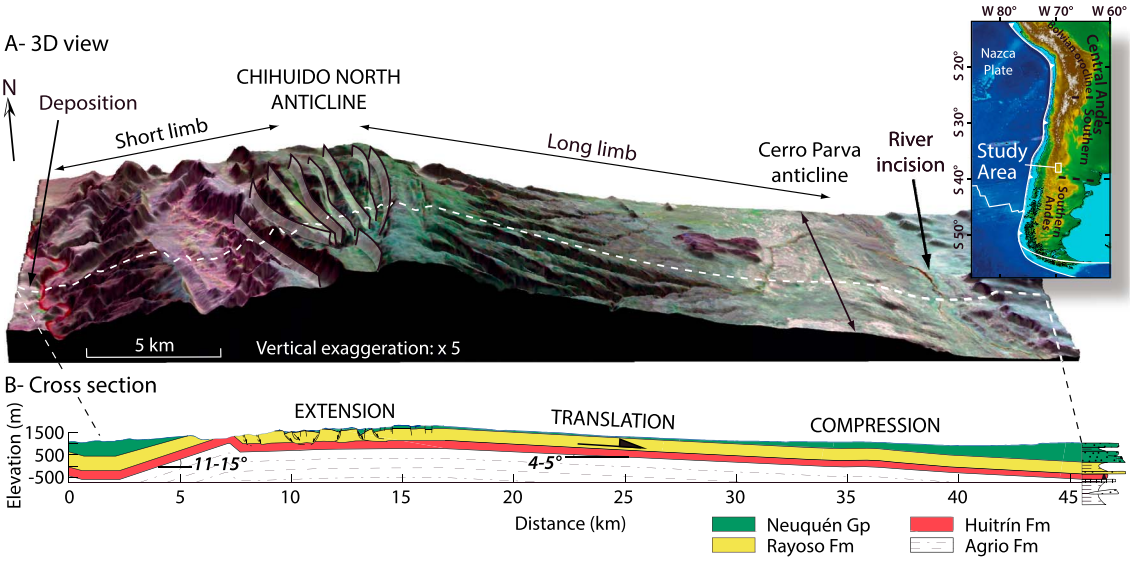

Figure 1. Gravity gliding on the Chihuido North anticline and its boundary conditions [modified from *Messager et al.*, 2014]. (a) Three-dimensional view of the Chihuido North anticline and interpretation of the thin-skinned structural pattern (Shuttle Radar Topography Mission Digital Elevation Model and Advanced Spaceborne Thermal Emission and Reflection Radiometer image). (b) Synthetic structural cross section through the gravity slide. Gliding occurs along the long limb of the Chihuido North anticline. River valley at the toe of the long limb may favor and control the position of the downslope contractional failure. On the contrary, sedimentation may inhibit the gliding.

account various values of incision, sedimentation, internal friction angle, and thickness of overburden. The solutions so obtained may also be applied to explain gravity-driven processes occurring at various scales.

2. Geological Case Study

Our models attempt to approximate the geometrical and rheological parameters of the Chihuido North anticline along the front flexure of the southern Andean fold-and-thrust belts of Argentina (Figure 1) [*Mosquera and Ramos*, 2006; *Messager et al.*, 2010, 2014]. This crustal-scale asymmetric anticline is N170° trending and 70 km long, with its western limb shorter and steeper (15 km, 15°W) than the eastern limb (30 km, 4°E). Fold activity initiated during the Late Cretaceous [*Cobbold and Rossello*, 2003] and continued episodically during the Miocene [*Mosquera and Ramos*, 2006] and Plio-Pleistocene [*Messager et al.*, 2010]. The anticline involves the Jurassic to Cretaceous sedimentary cover (Figure 2). Multiple décollement layers are made up of black shales belonging to the Los Molles Formation (Lower Jurassic) and the evaporites of the Auquilco Formation (Oxfordian) and the Huitrín Formation (Lower Cretaceous) [e.g., *Howell et al.*, 2005]. In the Chihuido North area, these formations are hundreds of meters thick and lie at depths of 4200, 3200, and 1000 m, respectively (Figure 2). Gypsum dominates the Auquilco evaporites, while halite predominates within the Huitrín Formation [e.g., *de Brodtkorb et al.*, 1982]. In the area of the Chihuido North anticline, the salt of the Huitrín Formation is ~150 m thick and is composed of 96–98% halite, interbedded with minor layers of anhydrite, gypsum, clays, and celestite [*Tezón et al.*, 1969; *Lyons*, 1980; *de Brodtkorb et al.*, 1982].

From structural and geomorphic observations, *Ramos* [1981] and *Messager et al.* [2014] found evidence for recent thin-skinned extensional and compressional structures trending N-S above the Chihuido North anticline (Figure 1). Extension developed at the outer hinge of the flexure, being expressed at the surface by a set of elongated and parallel valleys, 10–15 km long and 500 m wide. The valleys form endorheic basins filled by unconsolidated deposits. Normal faults bounding these elongated valleys reflect the presence at depth of rollovers and turtle back anticlines built above Cretaceous evaporites [*Messager et al.*, 2014]. These structures indicate the stretching and eastward displacement of a thin sheet of sedimentary cover. At the eastern toe of the anticline, the 30 km long and 5 km wide Cerro Parva anticline, which reaches 75 m in height and distorts the present-day drainage network, expresses thin-skinned shortening. The morphological imprint of the thin-skinned stretching and shortening domains suggests that their deformation is potentially coeval with the Plio-Pleistocene uplift of the Chihuido North anticline [*Messager et al.*, 2014]. Field and seismic surveys fail to reveal any internal deformation between these different domains. To reconcile the stretching and

©2014. American Geophysical Union. All Rights Reserved.

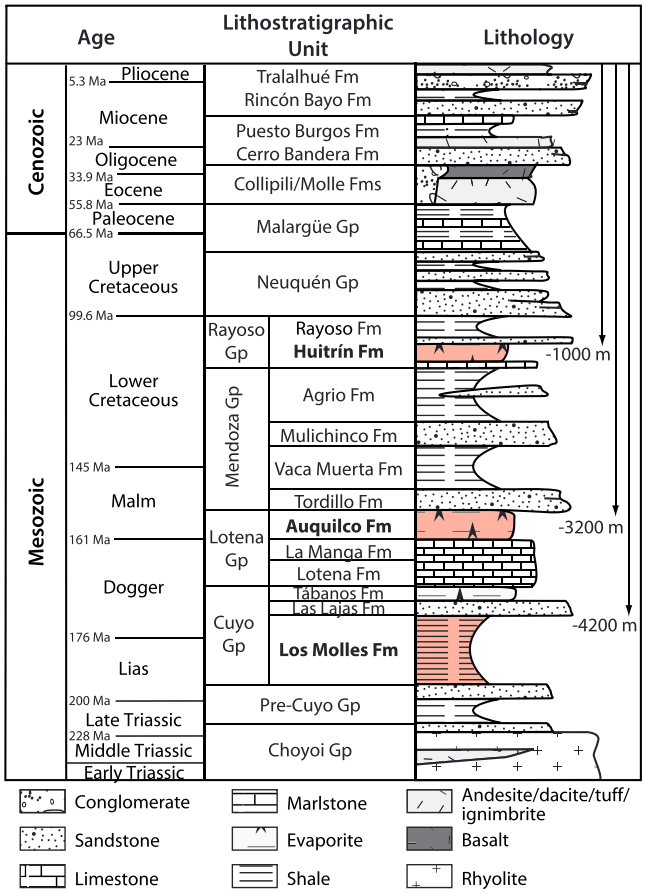

Figure 2. Stratigraphic column of the southern Neuquén Basin. After *Holmberg* [1964, 1976], *Zöllner and Amos* [1973], *Ramos* [1981], and *Leanza and Hugo* [1999] [modified from *Messager et al.*, 2010]. In bold are the potential décollement layers made of the evaporites of the Huitrín Fm. (~1000 m depth) and Auquilco Fm. (~3200 m depth), and the shales of the Los Molles Fm. (~4200 m depth). Fm, Formation and Gp, Group.

shortening deformation styles, *Messager et al.* [2014] assumed that rigid translation of the sedimentary cover took place down the long limb of the Chihuido North anticline according to a gravity gliding process. After reaching a thickness of around 1 km and a length of 30 km, the overburden mass slides above the 4–5°E dipping Cretaceous evaporites (Figure 1). The tilt of the basal décollement may have generated a sufficient slope to allow gravity gliding. However, the décollement occurs along the long limb of the Chihuido North anticline, where the structural slope is at a minimum (Figure 1). *Schultz-Ela and Walsh* [2002] and *Lacoste et al.* [2011] emphasized the importance of river incision and sedimentation in the initiation and localization of gravity gliding. At the eastern toe of the Chihuido North anticline, a 4 km wide and 200 m deep valley might have created a weak zone controlling the location of the downslope contractional failure. On the other hand, a 1000 m thick Cretaceous to Neogene depocenter is located on the Agua Amarga Pampa to the west of the Chihuido North anticline, along its short limb [*Leanza and Hugo*, 1999; *Zapata et al.*, 2003; *Cobbold and Rossello*, 2003]. The depocenter was incised during the Quaternary [*Messager et al.*, 2010]. This sedimentation might have increased the downslope failure resistance by thickening the overburden at the toe of the short limb, thus preventing gliding to the west where the slope is steepest.

In this study, we test numerically the roles of tectonic tilt, river incision, and sedimentation in controlling the initiation and location of onland large-scale gravity gliding.

3. Modeling Method and Parameters

3.1. Physical Problem

We consider a viscous décollement level overlain by a frictional-plastic overburden (sedimentary cover) of laterally uniform thickness (Figure 3). When the slope is sufficient, gravity drives the overburden downward, causing upslope extension and downslope contraction. The physical problem has been previously been addressed for gravity spreading in two dimensions by *Gemmer et al.* [2005] and for pure gravity gliding in three dimensions by *Mourgues and Cobbold* [2003]. These models considered a marine environment where the presence of water increases the solid and fluid pressure in sediments, thus reducing critically the effective stresses and the critical slope angle required to trigger instabilities. In addition, lateral friction hinders gliding dynamics and increases the critical slope. Our models assume continental environments without any effects of water loading, pore fluid pressure, or lateral friction. We consider upper and lateral surfaces to be stress free. We focus here on the critical conditions of slope instability as well as the location and intensity of deformation.

©2014. American Geophysical Union. All Rights Reserved.

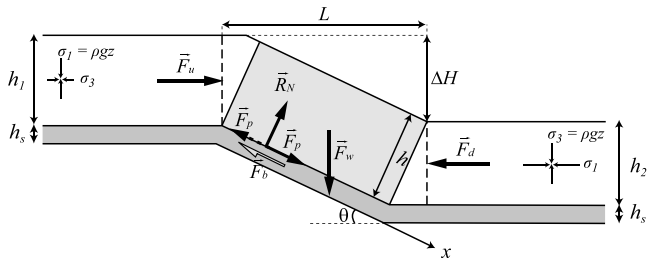

Figure 3. Analytical approach to solve the physical problem. Overburden is light grey and underlying décollement is dark grey. Geometrical and physical parameters: h_s: décollement thickness, h_1 and h_2: upslope and downslope overburden thicknesses, θ: slope angle, L: length of slide, ΔH: difference in elevation between the upslope and downslope of the raft, ρ: overburden density, and g: acceleration due to gravity. Forces acting on the overburden gliding zone: F_w: overburden weight, $\vec{F}_u$: upslope tension, $\vec{F}_d$: downslope contraction, $\vec{F}_p$: pressure-driven Poiseuille flow, $\vec{F}_b$: basal resistive force, $\vec{R}_N$: normal reaction force, σ_1: maximum compressive stress, and σ_3: minimum compressive stress. Note that $\vec{F}_p$ is directed upward if $h_1 < h_2$ or downward if $h_1 > h_2$.

The weight of the overburden ($\vec{F}_w$) and the upslope tension ($\vec{F}_u$) are the driving forces of the slide, while the contractional force ($\vec{F}_d$) offers resistance to the downslope failure (Figure 3). When the overburden fails and moves downslope, Couette flow gives rise to a basal resistive force ($\vec{F}_b$) in the viscous layer. In addition, the pressure-driven Poiseuille flow in the viscous layer produces shear traction on the base of the overburden, resulting in an increase of the slope-parallel force ($\vec{F}_p$).

F_u and F_d can be estimated by making the following assumptions: (1) far away from the tilted layer, the principal stress directions are horizontal and vertical in the upslope and downslope domains, respectively; (2) stress rotations are negligible, so these far-field stresses can be used in the expression of F_u and F_d; and (3) at the threshold slope angle θ_c at which the overburden starts gliding downward, the upslope region reaches the plastic yield point in an extensional regime, whereas the downslope reaches the plastic yield point in a compressional regime.

According to these assumptions and using the Mohr-Coulomb criterion which can be written as follows for a material at yield point:

$$\sigma_1(1 - \sin\phi) - \sigma_3(1 + \sin\phi) = 2c\cos\phi \tag{1}$$

where c is the cohesion. The stress state in the upslope domain is given by

$$\sigma_1 = \rho gz, \quad \sigma_3 = k\,\rho gz - 2c\alpha \tag{2}$$

while, in the downslope domain, the stress state is

$$\sigma_3 = \rho gz, \quad \sigma_1 = \frac{1}{k}\rho gz + 2c\beta \tag{3}$$

where $k = (1 - \sin\phi)/(1 + \sin\phi)$, $\alpha = \cos\phi/(1 + \sin\phi)$ and $\beta = \cos\phi/(1 - \sin\phi)$.

The resulting net forces (per unit length) F_u and F_d are then approximated by

$$F_u = \frac{1}{2}k\rho gh_1^2 - 2c\alpha h_1, \tag{4}$$

$$F_d = \frac{1}{2}k^{-1}\rho g{h_2}^2 + 2c\beta h_2 \tag{5}$$

where h_1 and h_2 are the upslope and downslope thicknesses of the overburden. Moreover, approximating the tilted domain by a parallelogram of length L and height h, the weight F_w (per unit length) can be roughly estimated by

$$F_w = \rho gLh. \tag{6}$$

By assuming that surface processes cause lateral changes in overburden thickness, the thin-sheet approximation [*Lobkovsky and Kerchman*, 1991] leads to an estimation of the Poiseuille flow in the viscous layer which is independent of viscosity and slope length [e.g., *Gemmer et al.*, 2005]:

$$F_p = \frac{1}{2}\rho gh_s(h_1 - h_2) \tag{7}$$

The basal friction associated with Couette flow is independent from the slope angle and the overburden thickness [e.g. *Gemmer et al.*, 2005]:

$$F_b = \eta\frac{Vc}{h_s}L \tag{8}$$

©2014. American Geophysical Union. All Rights Reserved.

Table 1. Physical Parameters of the Numerical Models

	Parameters	Elastoplastic	Viscoelastic
ρ	Density	2600 kg m^{-3}	2330 kg m^{-3}
E	Young's modulus	25 GPa	40 GPa
ν	Poisson's ratio	0.25	0.33
c	Cohesion	1 MPa	-
ϕ	Friction angle	26°	-
η	Effective viscosity	-	10^{18} Pa s

where η is the viscosity, h_s the décollement thickness, and V_c the velocity of the slide.

$\vec{F}_w$ increases with the length (L), thickness (h), and slope angle (θ) of the overburden (equation (6)), while $\vec{F}_u$ and $\vec{F}_d$ increase with the internal angle of friction (ϕ) and the thickness (h) (equations (4) and (5)). Other important parameters are the pore fluid pressure, which reduces the effective normal stress on the faults planes, and the resistive force $\vec{F}_b$ due to sliding. This latter parameter increases with the viscosity (η) and length (L) of the ductile layer but decreases as its thickness (h_s) increases (equation (8)). Thinning of the ductile layer increased its strength, thus leading to increase coupling between the overburden and the basal detachment. The resistive force $\vec{F}_b$ controls the kinematics of the slide; the velocity and the force are set to zero when the overburden does not move (equation (8)). $\vec{F}_p$ is directed toward the thinnest part of the overburden layer ($h_1 \neq h_2$), and the force is set to zero if there is no variation in the overburden thickness, i.e., no lateral pressure gradient ($h_1 = h_2$; equation (7) and Figure 3).

3.2. Numerical Formulation

To compute stress, strain, and velocity fields in the overburden layer, we use the Lagrangian finite element code ADELI to obtain thermomechanical modeling solutions. This code has been used in numerous geodynamical applications, both at crustal [e.g., *Vanbrabant et al.*, 1997; *Huc et al.*, 1998; *Berger et al.*, 2004; *Got et al.*, 2008] and lithospheric scales [e.g., *Lesne et al.*, 2000; *Bonnardot et al.*, 2008; *Neves et al.*, 2008]. Belonging to the same family as the FLAC [Fast Lagrangian Analysis of Continua; *Cundall and Board*, 1988] and Parovoz codes [*Poliakov and Podladchikov*, 1992; *Gerbault et al.*, 2009], ADELI is based on an explicit temporal finite difference approach associated with the dynamic relaxation method [*Underwood*, 1983]. Numerical and mechanical aspects of this code in a 2-D or 3-D context can be found in *Hassani et al.* [1997] and *Chéry et al.* [2001].

3.3. Constitutive Laws

In this study, we use realistic rheologies and boundary conditions of the sedimentary cover to model the steady state deformation, motion velocities, and the state of stress of the overburden layer. In elastic domains, we assume a classical linear relation between the strain rate (d) and the stress rate tensor ($D\sigma/Dt$), where D/Dt is the Jaumann time derivative (Hooke's law):

$$\frac{D\sigma}{Dt} = 2Gd + \lambda \mathrm{tr}(d)I \tag{9}$$

where λ and G are the Lamé parameters which express the relationship between the Young's modulus and the Poisson's ratio, tr the trace of the tensor, and I is the identity tensor [*Chéry et al.*, 2001]. Brittle deformation is approximated by the Drucker-Prager failure criterion, which involves pressure-dependent plastic yield stress:

$$f(\sigma) = J_2(\sigma) - \frac{6\sin\phi}{3 - \sin\phi}(\overline{\sigma} + c\cot\phi) < 0 \tag{10}$$

where $J_2(\sigma)$ is the deviatoric stress intensity, $\overline{\sigma}$ is the mean pressure, c is the cohesion, and ϕ is the internal friction angle [*Chéry et al.*, 2001]. Moreover, to model the viscous behavior of the décollement level in a sufficiently simple way, the linear Maxwell model is adopted:

$$\frac{D\sigma}{Dt} = 2Gd + \lambda \mathrm{tr}(d)I - \frac{G}{\eta}\mathrm{dev}(\sigma) \tag{11}$$

where dev is the deviatoric component of a tensor and η is the viscosity.

©2014. American Geophysical Union. All Rights Reserved.

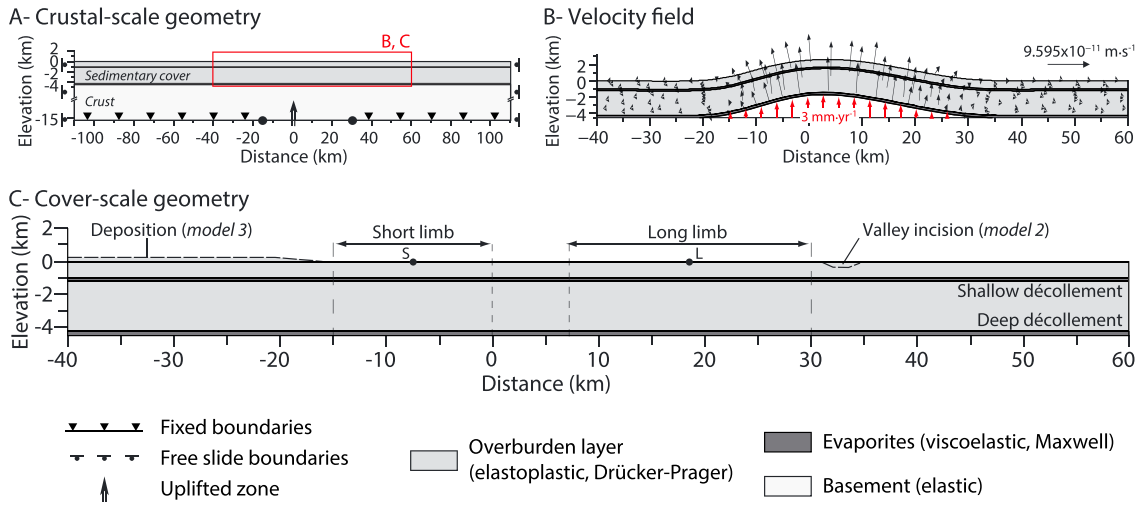

Figure 4. Numerical model settings: geometries and boundary conditions of the mechanical model. (a) Cross section at crustal scale. The crust is 10.6 km thick and exhibits elastic behavior. The sedimentary cover is compartmentalized into two elastoplastic layers (overburden: 1000 and 3000 m thick) and two viscoelastic layers (décollement), one at a depth of 1000 m (200 m thick) and the other at 4200 m (300 m thick). Displacement is locked along the two lateral edges. Along the basal edge, vertical displacement is imposed in the central part but is free between kilometer points −15 and +30 and locked elsewhere. This displacement generates an asymmetric anticline. (b) Lateral gradient of the vertical velocity at the base of the sedimentary cover. This induces a radial displacement field in the overburden. (c) Geometries of the three models. The reference model (*model 1*) does not have any lateral variation in geometrical or rheological properties. In *model 2*, river incision corresponds to a 4 km wide and 200 m deep trough at the toe of the long limb. In *model 3*, the upper elastoplastic is thickened to 200 m to simulate sedimentation at the toe of the short limb.

3.4. Rock Properties

Rheological parameters are summarized in Table 1. The shallow rocks involved in the Chihuido North anticline are made up of sandstones, shales, and limestones, which exhibit a brittle behavior according to an elastoplastic law (equation (10)). We use approximate mean values for the properties of these rock types, namely a Young's modulus of 25 GPa, a Poisson's ratio of 0.25 [*Turcotte and Schubert*, 1982], and a density (ρ) of 2600 kg m^{-3}. Experimental rock deformation showed that the cohesion (c) ranges from 0.3 MPa for shale to 36 MPa for limestone [*Hubbert and Rubey*, 1959; *Handin*, 1966]. We adopt a value of 1 MPa since it is known to be a good average for this mixture of rock types [*Schultz-Ela and Walsh*, 2002]. Typical friction angles are 15–30° for shales, 35–50° for limestones, and 26–56° for sands, which leads us to apply an average value of 26°. Marine gravity models generally use lower values of sediment density (2300–2500 kg m^{-3}) and friction angle (5 to 20°) [*Gemmer et al.*, 2005; *Gradmann et al.*, 2009]. The impact of ϕ values is discussed further below.

The evaporites can be considered as a mixture of salt rocks (halite, gypsum, or anhydrite) and shales, along with some minor limestones. We therefore choose an average density of 2330 kg m^{-3}, which is slightly higher than the value for pure gypsum. Over long time scales, typical rock salt deforms as a Newtonian fluid without any yield strength, while its instantaneous response is elastic. Despite impurities of anhydrite, gypsum, celestite, and clays within the salt layer, the role of a potential small finite yield strength that limits the detachment acting along the base of the slide is considered negligible. It is assumed that the halite of the Huitrín Formation has a purely viscous behavior and all potential décollement layers as purely viscous in order to compare equally their role on the gliding. Thus, we use the viscoelastic law to model this material (equation (11)). The effective viscosity of natural halite ranges from 10^{17} to 10^{18} Pa s [*van Keken et al.*, 1993]. We choose the upper end of this range to take nonsalt components into account. Similarly, we chose conservative values for the elastic bulk modulus of 40 GPa, as expected for gypsum rocks, while the Poisson's ratio is taken as equal to 0.33.

3.5. Model Geometry and Boundary Conditions

The models simulate a 15 km thick cross section of the upper crust capped by a 4.5 km thick sedimentary cover (Figure 4a). The top of this cover is initially set at an elevation of 0 m. Displacements are horizontally locked but vertically sliding freely along the two lateral edges. At the bottom of the model, displacements are locked to the left of km point −15 and to the right of km point +30. We set a vertical displacement at

©2014. American Geophysical Union. All Rights Reserved.

the bottom center of the model (Figure 4a). These settings generate a lateral gradient in the vertical displacement, which reaches a maximum of 3 mm yr^{-1} at km 0 (Figure 4b). This value is unrealistically high for the tectonic setting studied here. However, our goal is not to model the kinematics of deformation and we only need to make sure that this value does not modify the critical slope required to trigger the instability (θ_c). As a result, we obtain a crustal-scale and asymmetric bulge similar to the Chihuido North anticline. The short limb is 15 km wide on the left, and the long limb is 22 km wide on the right, with a gently dipping zone up to 8 km long at its apex. The lateral edges of the model are sufficiently far from the uplifted domain (around 70 km) not to influence significantly the results.

To match the sedimentary column (Figure 2), we set up the sedimentary cover that consists of four layers, including two décollements, with no lateral variations in geometry or rheology. The uppermost décollement is 200 m thick with its top at a depth of 1 km (Figure 4c). The second décollement is 300 m thick and forms the base of the sedimentary cover at 4.2–4.5 km in depth. We use a 2-D finite element mesh, which is finer in the overburden than in the décollement layers, while also checking that the element mesh size is small enough to provide a precise analysis.

Model 1 is the reference model, without any incision or sedimentation. *Model 2* takes into account fluvial incision at the toe of the long limb. In this way, we create a 4 km wide and 200 m deep trough in the overburden at km +32 (see Figure 4c), as observed at the eastern toe of the Chihuido North anticline (Figure 1). *Model 3* investigates the role of sedimentation at the toe of the short limb. This latter model does not attempt to represent the total thickness of the Agua Amarga depocenter, since it has subsequently been eroded. We therefore thicken the upper elastoplastic layer to simulate a 200 m thick sedimentary basin on the left side of the model. This value is of a similar order of magnitude as the incision, allowing us to compare the impact of these two surface processes in gliding dynamics.

The simulations are run over 1.33 Myr with a total of 4.2×10^6 time steps using around 5×10^3 three-noded finite elements per layer. At the end of the simulations, we analyze the cumulative shear strain corresponding to the second invariant of the deviatoric strain, as well as the distribution of stress and cumulative displacements in the overburden layers. We determine the displacement field by comparing the resulting geometries of the three models with a model without décollement layers (viscoelastic layers), i.e., without gravity slides (*model 0*). Thus, we can exclude displacements related to the uplift gradient, which is the same in both configurations, keeping only the gliding component of the displacement field. We then derive the critical conditions of gliding by plotting the displacements of two points along the short (S) and long (L) limbs (Figure 4c), between two time stations and as a function of the slope. Gliding starts when the displacements are nonzero.

4. Numerical Results

4.1. Reference Model (*Model 1*): Without Any Incision or Sedimentation

4.1.1. Geometry

At the end of the simulation, the bulges in *model 0* and *model 1* differ only at their apices (Figure 5): the top reaches 2640 m in *model 0* and 2490 m in *model 1*. This results from the collapse of the top of the sedimentary cover above the shallowest décollement layer in *model 1*. This collapse generates an 11 km wide and 150 m deep trough (grey shading in Figure 5a). The topographic surface shows a set of scarps with an elevation of 25 to 150 m, which delimit subsidiary hills and troughs (inset in Figure 5b). The contact between the shallowest elastoplastic and viscoelastic layers is also irregular at the hinge of the bulge, but the roughness shows an amplitude of less than 25 m.

4.1.2. Cumulative Shear Strain Field

Figure 5 shows the cumulative shear strain field (second invariant of the deviatoric strain tensor), with blues and reds indicating low and high strains, respectively, without reference to the strain regime (extensional or compressional). Deformation is compartmentalized by the four layers of the model. Viscoelastic layers concentrate high cumulative strain (0.3–1.0), as expected in the basal hinges of the deepest layer. The elastoplastic layer shows high cumulative strain (0.3–1.0) in the collapsed area (km −1 to +7 in Figure 5b). In detail, the strain field is segmented by a set of four steep conjugate strain zones that cut right through the layer (Figure 5b). These zones link the topographic scarps to the highly deformed domains of the shallowest viscoelastic layer. Cumulative strain exceeds 1.0 in the central part of the trough and decreases laterally. These conjugate zones delimit less intensely deformed domains labeled B1 to B4 in Figure 5b. The flanks of the bulge are not deformed. Two areas

©2014. American Geophysical Union. All Rights Reserved.

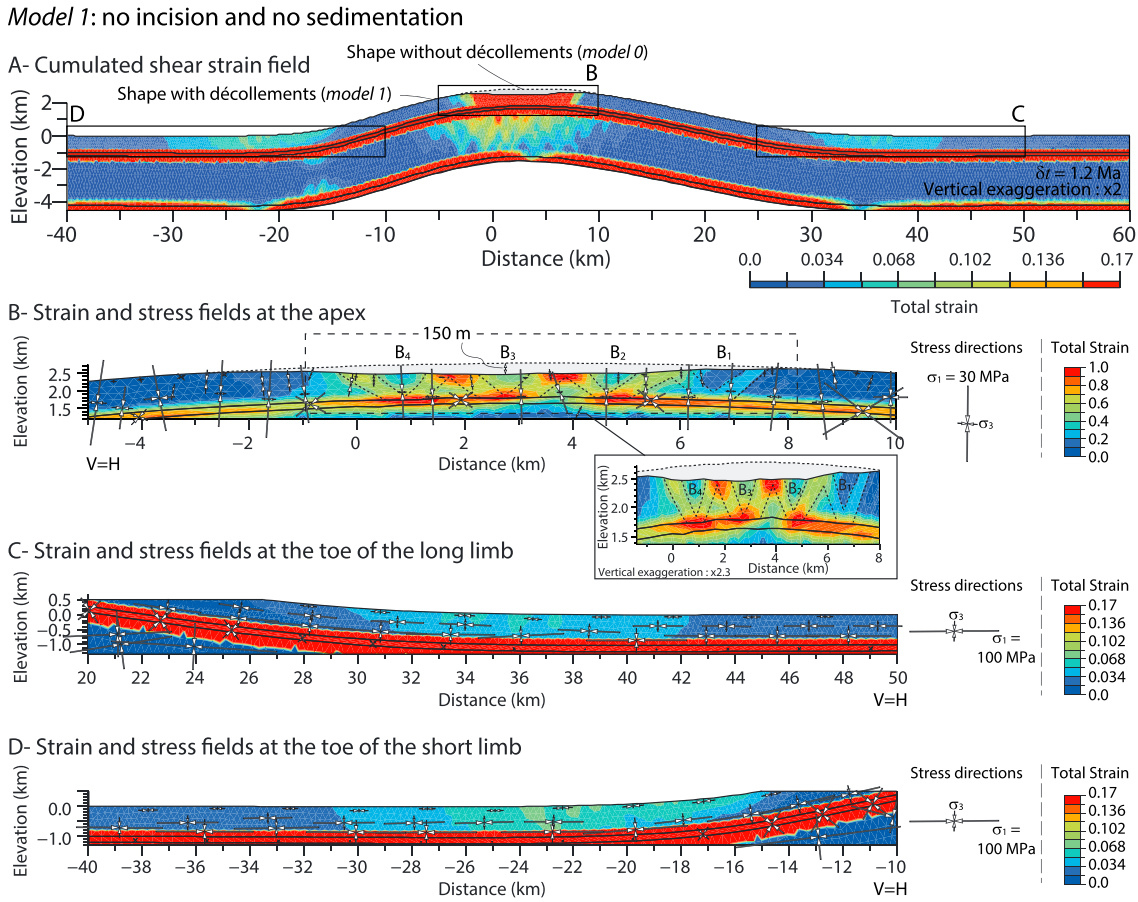

Figure 5. *Model 1* without incision or sedimentation: (a) cumulative shear strain and deviatoric stress fields after 1.2 Myr at the scale of the sedimentary cover, with zooms in (b) the upper elastoplastic layer at the apex of the bulge, and at the toes of the (c) long and (d) short limbs. B1 to B4: four individual collapsed blocks accommodating the collapse at the top hinge of the bulge.

of low cumulative strain are located at the toes of the bulge (Figure 5a). At the toe of the long limb, deformation is mainly concentrated between km +30 and +42, where cumulative strain reaches only 0.051 in the elastoplastic layer (Figure 5c). At the toe of the short limb, cumulative strain is slightly higher (0.085) in a 15 km wide area (km −30 to −15; Figure 5d). The cumulative strain decreases outward and reaches 0.03 as far as 15 km away from the downslope edge of the limbs (Figure 5a). The deep elastoplastic layer shows mainly intermediate cumulative strain (<0.136) at the upper hinge of the bulge where strain is radial. Weakly deformed areas (<0.068) are also recorded in the syncline hinges of the bulge (Figure 5a).

4.1.3. Stress Field

Figure 5 presents the magnitudes and orientations of the principal stresses σ_1 and σ_3. To a first order of approximation, σ_1 is vertical in the two elastoplastic layers above the uplifted area and is correlated with the cumulative shear strain (Figures 5b–5d). In this domain, σ_1 reaches a value of 5–20 MPa (Figure 5c). Near the surface, the stress regime could be extensional, indicating minor tension, with stresses lower than 3 MPa. In the areas of low cumulative strain at the toes of the bulge, σ_1 is horizontal and ranges between 20 and 100 MPa from the top to the base of the elastoplastic layer (Figures 5c and 5d). Elsewhere in the elastoplastic layers, the stress field is isotropic and corresponds to the lithostatic pressure. Although the stress field is isotropic in the viscoelastic layers, its orientation is nevertheless oblique to the layers (Figures 5b–5d).

4.1.4. Displacement Field

Figure 6 illustrates the cumulative displacement field. Displacements of less than 15 m in the deep elastoplastic layer are negligible and are related to numerical noise (Figure 6a). Displacements are concentrated in the shallow elastoplastic layer between kilometers −40 and +60, being approximately parallel to the layers and directed outward from the apex of the bulge (Figure 6a). Displacements are maximal at the apex of the bulge,

©2014. American Geophysical Union. All Rights Reserved.

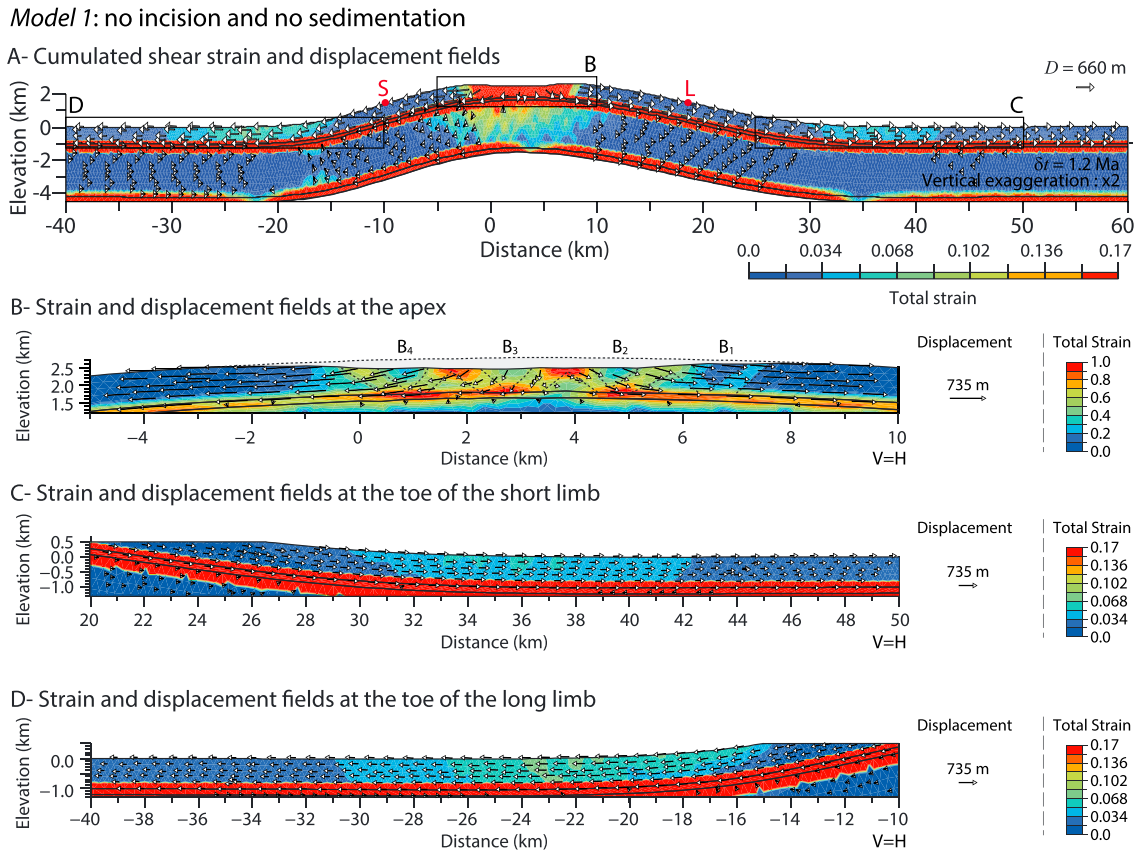

Figure 6. *Model 1* without incision or sedimentation: (a) cumulative shear strain and displacement fields after 1.2 Myr at the scale of the sedimentary cover, with zooms in (b) the upper elastoplastic layer at the apex of the bulge, and at its (c) right and (d) left toes.

where they range between 400 and 660 m and then decrease along the limbs (300–400 m) and in the syncline hinges (300–450 m). Displacements gradually decrease away from the toe of the limbs to be null along the lateral edges of the model indicating that the displacement is absorbed by the strain. The displacement vectors display a variable orientation in space. At the apex of the bulge, the displacement field is radial outward: displacement vectors are strongly oblique to the layers and directed downward, with a progressive flattening away from the center (Figure 6b). Correlated with the trough, these vectors reflect the collapse and the lateral escape of the cover on top of the bulge. Moreover, these displacements involve the top of the shallow viscoelastic layer but not its base. Therefore, the collapse reaches only the shallow ductile layer (Figure 6b). At the toes of the bulge, vectors tend to be oblique to the top of the elastoplastic layer (Figures 6c and 6d). Although this could result from a slight uplift, such a process is not observed in the model.

4.1.5. Characterization of Gravity Gliding

The cumulative shear strain is correlated with the deviatoric stress regime, with the highest strain being concentrated in the hinges of the bulge. The lack of displacements in the deep elastoplastic layer shows that deformation is not related to the gliding component. The flexural bending due to uplift would produce this shear strain, which has extensional and compressional components within the external and internal hinges of the bends, respectively. Stretching is increased since the lateral edges of the model are laterally locked.

Model 1 shows that high cumulative strain is correlated with an irregular displacement field in the shallow elastoplastic layer. This reflects thin-skinned tectonics related to extensional and/or compressional forcing. Above the bulge, the stress regime is extensional (vertical σ_1 and horizontal σ_3). The cumulative strain is maximal, and the displacement vectors express a collapse and a lateral escape. Stretching is accommodated by a set of conjugate strain zones that act as conjugate normal faults. Four collapsed blocks (B1–B4) are generated with increasing maturity toward the center of the hinge (Figure 5). These faults root in the shallow viscoelastic layer. Along the limbs of the bulge, displacement vectors in the elastoplastic layer are oriented

©2014. American Geophysical Union. All Rights Reserved.

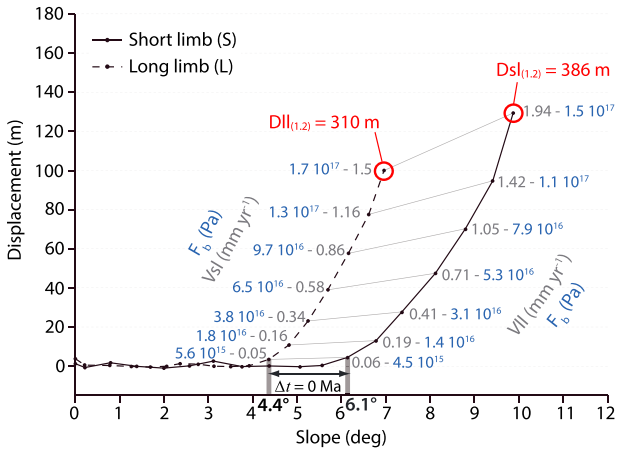

Figure 7. *Model 1* without incision or sedimentation: displacements every 66,590 years as a function of slope. Displacements are estimated for two points S (short limb) and L (long limb) located in the middle of each limb of the bulge (Figure 4), which cancels out the extensional and compressional components of the gliding. We consider that the critical slope θ_c of the gravity gliding is attained when the displacement is nonzero. The delay of initiation of the slide is Δt, with its onset occurring at the same time above both limbs. In blue are the values of F_b at each time step and in grey are V_{sl} and V_{ll} the velocities of gliding along the short and long limbs, respectively. $Ds_{l(1.2)}$ and $Dl_{l(1.2)}$ are the cumulative displacements after 1.2 Myr along the short and long limbs, respectively: displacement is greater above the short limb.

parallel to the shallow viscoelastic layer, and no strain is recorded. Hence, the limbs correspond to undeformed rigid rafts that slide down the slope and transfer stretching from the apex of the bulge to low-strain areas farther downslope. In these areas, the compressive stress regime coupled with outward directed displacements reflects a diffuse shortening that does not generate uplift. This pattern shows that the shallow viscoelastic layer acts as a décollement and that gravity gliding occurs above the bulge. *Model 1* implies that gravity gliding could occur on land with realistic rheologies and no pore fluid pressure.

Deformation in the shallow elastoplastic layer results from flexural and gravity-driven processes. At first, crustal uplift generates flexural stretching and contraction in the sedimentary cover. Then, sliding of the overburden is initiated when the basal décollement layer reaches a critical slope. Tilting of the basal décollement in our model does not reach the critical slope to allow gliding of the deep elastoplastic layer. Since both décollements have the same rheological properties, these results highlight the role of overburden thickness. Strain related to the flexure is negligible (~7 times less) compared to the strain generated by sliding. Thus, we argue the overburden at either the top or bottom of the slope does not fail owing to the stress developed by flexure during the uplift phase.

4.1.6. Critical Slopes and Amount of Displacement Related to Gravity Gliding

Several parameters play a role in the initiation of gravity gliding. The weight $\vec{F}_w$ of the overburden increases with the length (L) and slope angle (θ) of the limb (equation (6)). Therefore, it is difficult to predict which limb of the asymmetric bulge is more favorable for gliding. To address this point, we compare the critical slope angle (θ_c) required to trigger the instability, the delay of initiation (Δt), the velocity (V), and the cumulative displacement (D) of the slides occurring along both limbs. Since the displacement and the strain intensity are negligible along the lateral edges the model, we argue that the boundaries do not constrain the values of the critical slope, the intensity, and the kinematics of the gravity gliding.

For this purpose, we estimate the displacements of two points located in the middle part of each limb (S and L in Figure 6a). These undeformed domains, which are only translated down the slope, do not involve the extensional and compressional components of the displacement. Sliding initiates when S and L start to move. Figure 7 shows the displacement of S (solid line) and L (dashed line) as a function of the slope angle. We compute the cumulated displacements at each time step (δt) of the simulation. The slope angles of the short and long limbs range from 0 to 10.4° and from 0 to 7.4°, respectively.

Gliding initiates for a lower slope along the long limb (4.4°) than along the short limb (6.1°) (Figure 7). Even if the critical slope angle is lower for the long limb, gliding occurs at the same model run time (δt = 0.8 Myr) on each limb (Δt = 0 Myr). This shows that $\vec{F}_w$ exceeds the resistive forces at the same time on both limbs. Initiation of gliding requires a steeper slope along the shorter limb. The cumulative displacement is greater along the shorter limb ($D_{sl} = 386$ m $> D_{ll} = 310$ m) where the slide is faster (Figure 7). According to the equation (8), the resistive force is around 1.25 times lower along the shorter limb (F_b in Figure 7). The shorter limb thus facilitates the gliding.

©2014. American Geophysical Union. All Rights Reserved.

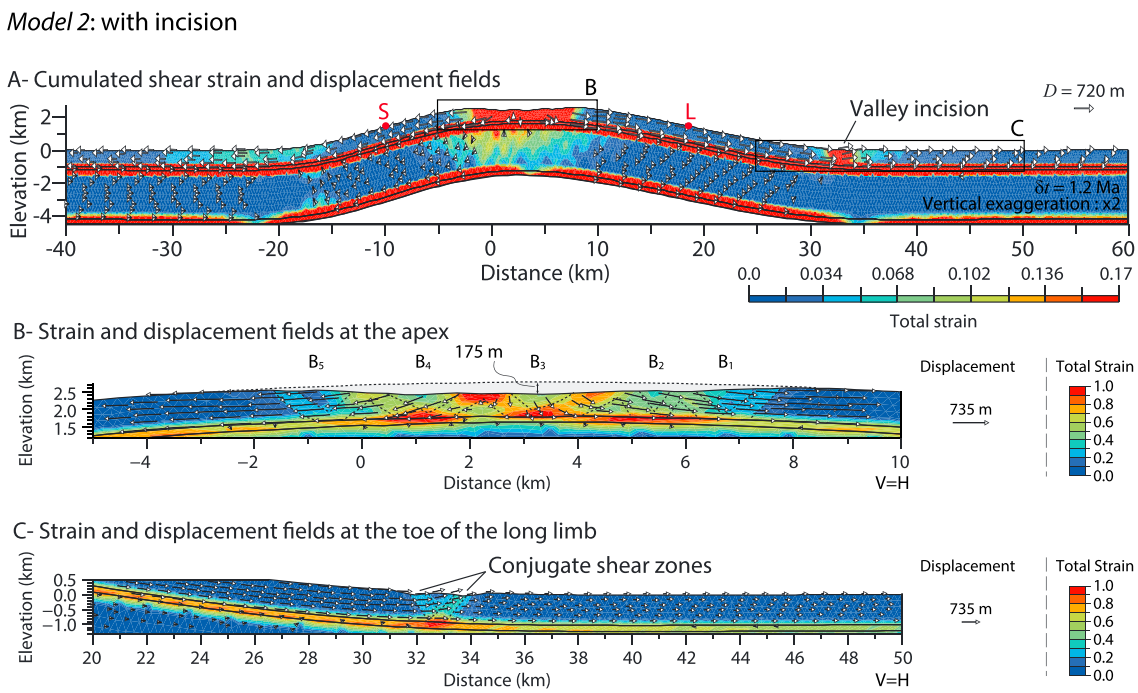

Figure 8. *Model 2* with incision: (a) cumulative shear strain and displacement fields after 1.2 Myr at the scale of the sedimentary cover, with zooms in (b) the upper elastoplastic layer at the apex of the bulge, and at its (c) right toe.

While simulated gravity gliding is concurrent above both limbs, it is more intense and faster along the short limb. Although gliding would appear to be easier above the short limb, this is contradicted by field observations (Figures 1 and 6). Indeed, gliding has been observed only along the long limb of the Chihuido North anticline.

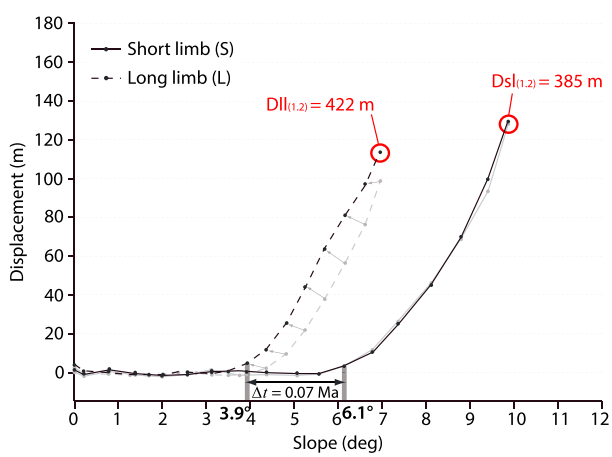

Figure 9. *Model 2* with incision: displacements every 66,590 years as a function of slope. Displacements are estimated for two points S (short limb) and L (long limb) located in the middle of each limb of the bulge (Figure 4), which cancels out the extensional and compressional components of the gliding. We consider that the critical slope θ_c of the gravity gliding is attained when the displacement is nonzero. The delay of initiation of the slide is Δt, with its onset occurring first along the long limb. $D_{sl_{(1.2)}}$ and $D_{ll(1.2)}$ are the cumulative displacements after 1.2 Myr along the short and long limbs, respectively: displacements are greater along the long limb.

4.2. Interaction Among Incision, Sedimentation, and Gravity Gliding

In this section, we investigate separately the impact on gravity gliding of fluvial incision (*model 2*) and sedimentation (*model 3*) at the toes of the bulge. We focus our analysis on the shallowest elastoplastic and viscoelastic layers.

4.2.1. Impact of a River Valley at the Toe of the Long Limb (*Model 2*)

Figure 8 shows the cumulative shear strain and displacement fields obtained in *model 2*. Cumulative strain along the short limb is the same as obtained in *model 1* (Figure 8a). Stretching is more intense at the apex of the bulge. In this case, stretching is accommodated by five conjugate fault systems (B1–B5; as against four in *model 1*; Figure 6). The cumulative strain exceeds 1.0 and the magnitude of vertical collapse increases to 175 m (Figure 8b; as against 150 m in *model 1*). At the toe of the long limb, cumulative shear strain is mainly concentrated between two conjugate zones,

©2014. American Geophysical Union. All Rights Reserved.

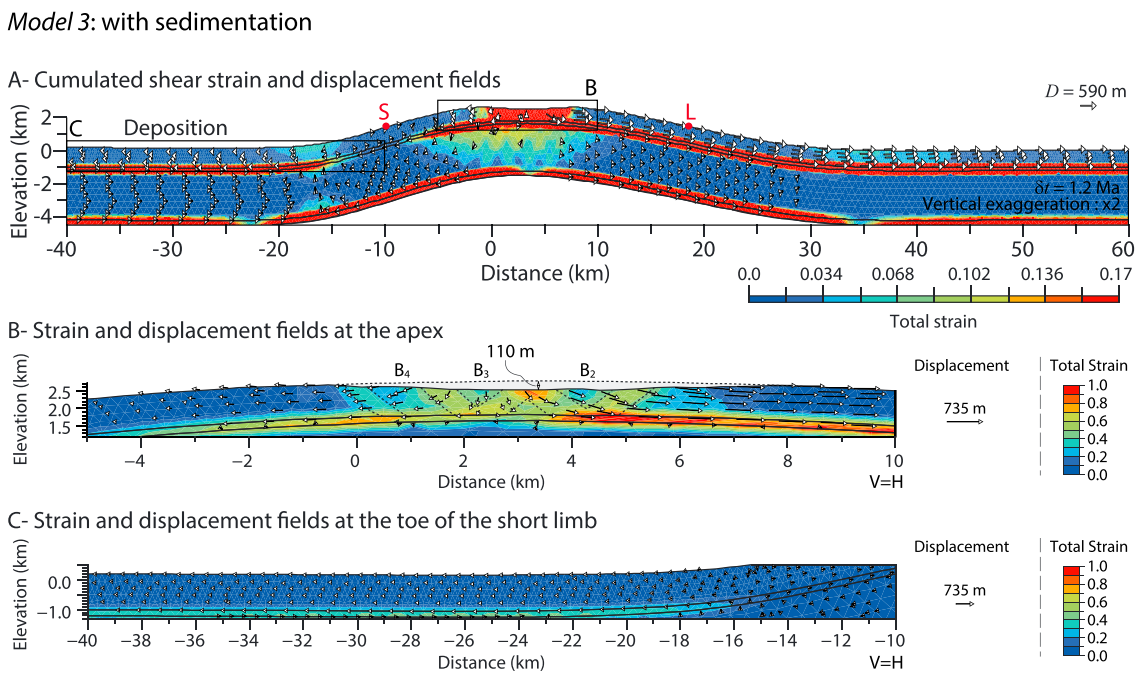

Figure 10. *Model 3* with sedimentation: (a) cumulative shear strain and displacement fields after 1.2 Myr at the scale of the sedimentary cover, with zooms in (b) the upper elastoplastic layer at the apex of the bulge, and at its (c) left toe.

located in a 3 km wide area in the valley (Figures 8a and 8c). These zones link the border of the valley to the highly deformed area of the viscoelastic layer. The valley floor and the top of the viscoelastic layer are both warped (Figure 8c). Beneath the valley, displacement vectors are oblique and face upward. To the right of the valley, displacements are parallel to the shallow viscous layer and have lower vector magnitudes. The valley floor is uplifted, and the strain zones may undergo reverse faulting rooted in the shallow décollement layer. Thus, the valley concentrates most of the shortening. In this case, the critical slope angle is 3.9° above the long limb (Figure 9). Gliding initiates earlier above the long limb (time station δt = 0.73 Myr, as against δt = 0.8 Myr) and the cumulative displacement is greater at the end of the simulation (D_{ll} = 422 m > D_{sl} = 385 m).

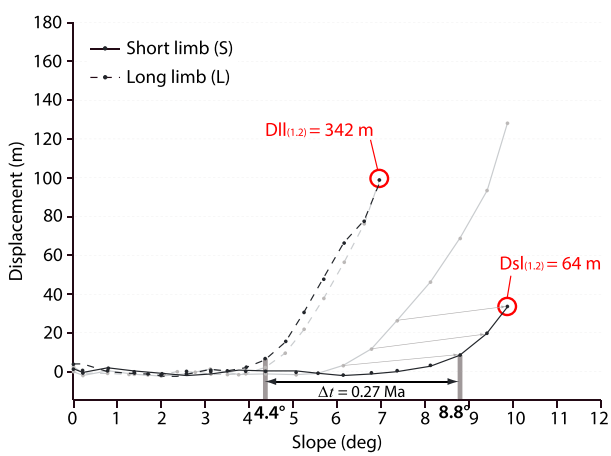

Figure 11. *Model 3* with sedimentation: displacements every 66,590 years as a function of slope. Displacements are estimated for two points S (short limb) and L (long limb) located in the middle of each limb of the bulge (Figure 4), which cancels out the extensional and compressional components of the gliding. We consider that the critical slope θ_c of the gravity gliding is attained when the displacement is nonzero. The delay of initiation of the slide is Δt, with its onset occurring first along the long limb. $D_{sl_{(1.2)}}$ and $D_{ll_{(1.2)}}$ are the cumulative displacements after 1.2 Myr along the short and long limbs: displacements are greater along the long limb.

4.2.2. Impact of Deposition at the Toe of the Short Limb (*Model 3*)

In *model 3*, we thicken the upper elastoplastic layer to 200 m at the toe of the short limb (Figure 10). With respect to *model 1*, we do not observe any variation along the long limb (Figure 10a). Stretching at the apex of the bulge is narrower and displays only three collapsed blocks (B2–B4; four in *model 1*). The collapse reaches only 110 m in height (as against 150 m in *model 1*; Figure 5), and cumulative shear strain is lower than 0.8 (Figure 10b). Cumulative displacement is highly asymmetric and reaches a maximum above the long limb. At the toe of the short limb, strain is concentrated in the hinge of the bend, with low values of cumulative shear strain (<0.085) (Figure 10a). No strain is recorded elsewhere (Figure 10c).

©2014. American Geophysical Union. All Rights Reserved.

Gliding initiates later along the short limb (δt = 1.07 versus 0.8 Myr), with a critical slope angle 2 times steeper (θ_c = 8.8°) than along the long limb (θ_c = 4.4°) (Figure 11). Cumulative displacement along the short limb (D_{sl} = 64 m) is low in comparison with the long limb (D_{ll} = 342 m).

4.2.3. Failure Criterion for the Gravity Gliding

Models 2 and *3* simulate the impact of a small variation of the overburden thickness at the toes of the anticline. Theory suggests that the resistive force to downslope failure ($\vec{F}_d$) decreases with thinning (erosion) of the overburden and increases with its thickening (deposition). This would favor gravity gliding above the long limb and would delay it above the short limb.

Indeed, in comparison with the reference model, the presence of a valley decreases the critical slope angle required to trigger instabilities and increases the cumulative displacement. The apical stretching is thus increased, which results in an additional collapsed block (B5) (Figure 8b). Reverse faulting accommodates most of the shortening near the valley (Figure 8c). Thus, this valley creates a weakness zone that facilitates the initiation of gliding, increasing the upslope stretching of 35% and controlling the location of downslope shortening.

On the contrary, sedimentation increases the critical slope angle and reduces the cumulative displacements of 85%. The apical stretching is strongly reduced in comparison with *model 1*, as expressed by the lack of collapsed block B1 (Figure 10b). In addition, shortening at the toe of the limb is very weak, and strain in the syncline hinge may be fully explained by flexural bending (Figures 10a and 10d). Thus, deposition strengthens the overburden and inhibits the gravity gliding.

Considering a mixed model taking into account incision and deposition, gravity gliding would occur only along the long limb where the slope angle is less than 5.2° with a critical slope angle reduced to 3.9°. *Models 2* and *3* show that gravity gliding could be favored above the long limb while it is negligible above the short limb, which runs against the prediction of *model 1* with constant overburden thickness.

5. Analytical Solutions of Gravity Gliding

We compare the numerical models with an analytical theory to discuss how the critical slope depends on (1) the length of the slide, (2) the thickness of the overburden, (3) the depth of incision, and (4) the thickness of sedimentation. We also discuss the influence of the internal angle of friction. We consider the décollement layer as a pure viscous body and we do not investigate the kinematics of the gliding after the critical slope angle is reached. Thus, the analytical approach assumes that the basal detachment does not act against the gliding, irrespective of the slope angle. The discrepancy between the numerical model and the analytical results may be due to inaccuracies in the thin-sheet approximation assumed in the analytical approach.

5.1. Estimation of Critical Slope Angle

In this section, we provide a direct and rough estimate of the critical slope angle θ_c above which instability can occur. This is achieved by solving a simplified two-dimensional equilibrium problem, to obtain results that can be compared with our numerical models and used to facilitate the analysis of some parameter effects. Contrary to the analytical work of *Dahlen* [1984] and *Xiao et al*. [1991] and the recent analytical theories of *Gemmer et al*. [2005], *Mourgues and Cobbold* [2006], *Brun and Fort* [2011], and *Mourgues et al*. [2014], our analytical approach assumes continental environments with no additional solid or pore fluid pressure in the sediments. Moreover, there is no lateral friction since we are considering lateral free edges.

For this purpose, let us consider the equilibrium of the tilted domain shown in Figure 3. Since the body is at rest, the basal Couette force ($\vec{F}_b$) falls to zero. Thus, the only forces acting on this domain are its weight $\vec{F}_w$, the reactions on its lateral faces $\vec{F}_u$ and $\vec{F}_d$, and the reaction on its base (normal reaction $\vec{R}_N$ and Poiseuille force $\vec{F}_p$).

The projection of the momentum equation $\vec{F}_u + \vec{F}_d + \vec{F}_w + \vec{R}_N + \vec{F}_p = \vec{0}$ onto the slope direction *Ox* gives the equilibrium condition:

$$(F_u - F_d)\cos\theta + F_w \sin\theta + F_p = 0 \tag{12}$$

where F_u, F_d, F_w, and $|F_p|$ are the norms of the corresponding vectors.

©2014. American Geophysical Union. All Rights Reserved.

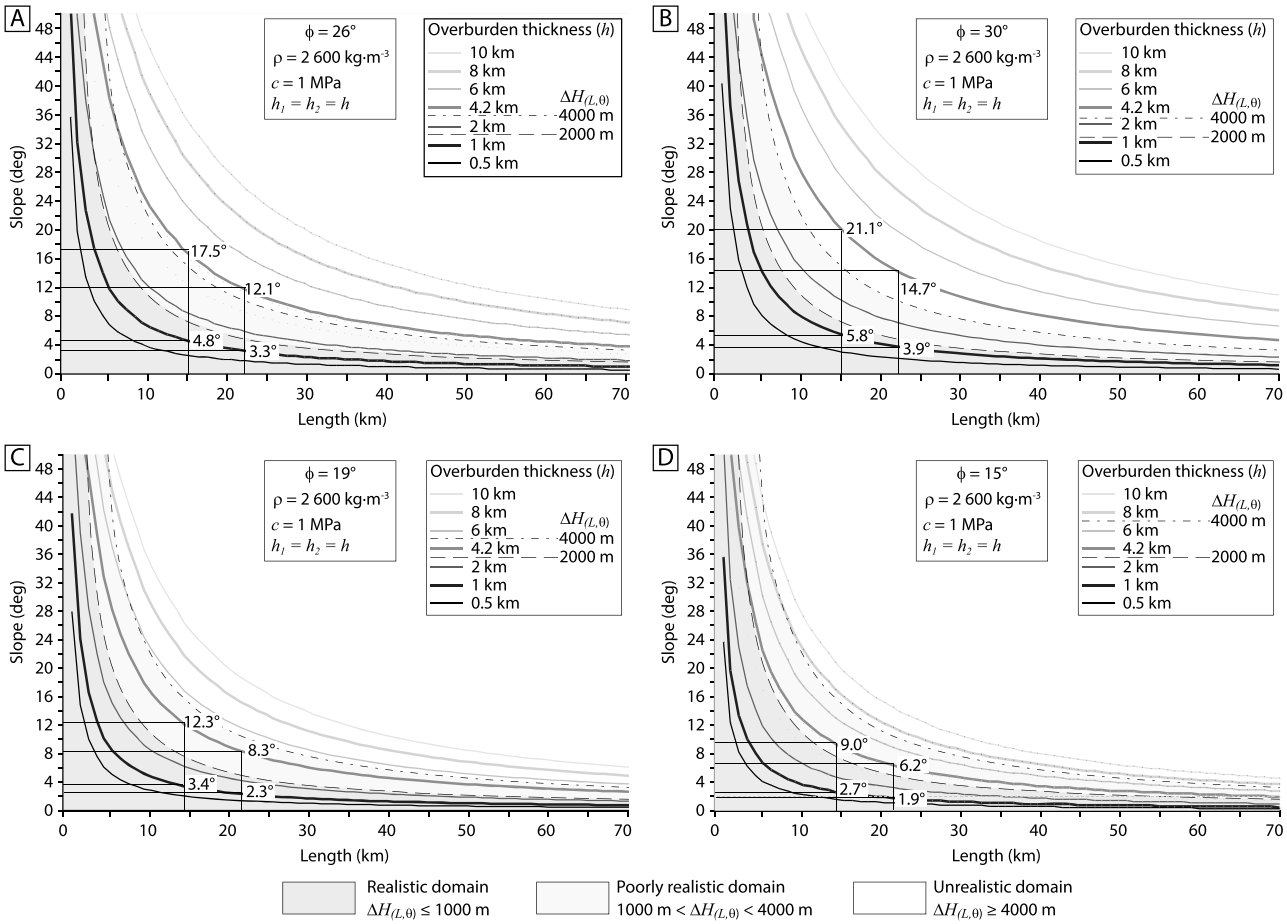

Figure 12. Results of the analytical model without incision or sedimentation: critical slope for sliding, as a function of the length of the sliding sheet (L), for various values of overburden thickness (h) with internal friction angles (ϕ) of (a) 26°, (b) 30°, (c) 19°, and (d) 15°. $\Delta H_{(L,\theta)}$: difference in height as a function of slope and sheet length.

The required expression for the critical slope angle θ_c is obtained by rewriting equation (12) with $\theta = \theta_c$, which gives

$$\Delta F \cos\theta_c + F_w \sin\theta_c + F_p = 0 \tag{13}$$

where $\Delta F = Fu - Fd$. Note that if $h_1 = h_2$ then the Poiseuille force F_p is zero and the solution is simply given by

$$\tan\theta_c = -\frac{\Delta F}{F_w} \tag{14}$$

whereas, when $h_1 \neq h_2$, equation (14) can be transformed into a quadratic equation involving $\tan(\theta_c/2)$:

$$\left(F_p - \Delta F\right) \tan^2(\theta_c/2) + 2F_w \tan(\theta_c/2) + \left(F_p + \Delta F\right) = 0 \tag{15}$$

which is solved for θ_c in $[0, \pi/2]$.

Compared to the solution of *Brun and Fort* [2011], our analytical approach takes into account the global equilibrium of the forces including the upslope and downslope forces. It also avoids the load of the sea water layer and considers lateral variations in the overburden thickness which implies the addition of the Poiseuille force at the base of the system.

5.2. Relations Between Length, Thickness, and Slope of Overburden

Figure 12 shows some analytical solutions of the critical slope angle as a function of the length and thickness of the slide. Few examples of inferred onland gravitational collapses may exceed 100 km long and 10 km thick [e.g., *Rangin et al.*, 2010]. In the following sections, we plot and discuss the results for lengths between 1 and 70 km and thicknesses between 0.5 and 10 km. This allows us to estimate the critical conditions for the

©2014. American Geophysical Union. All Rights Reserved.

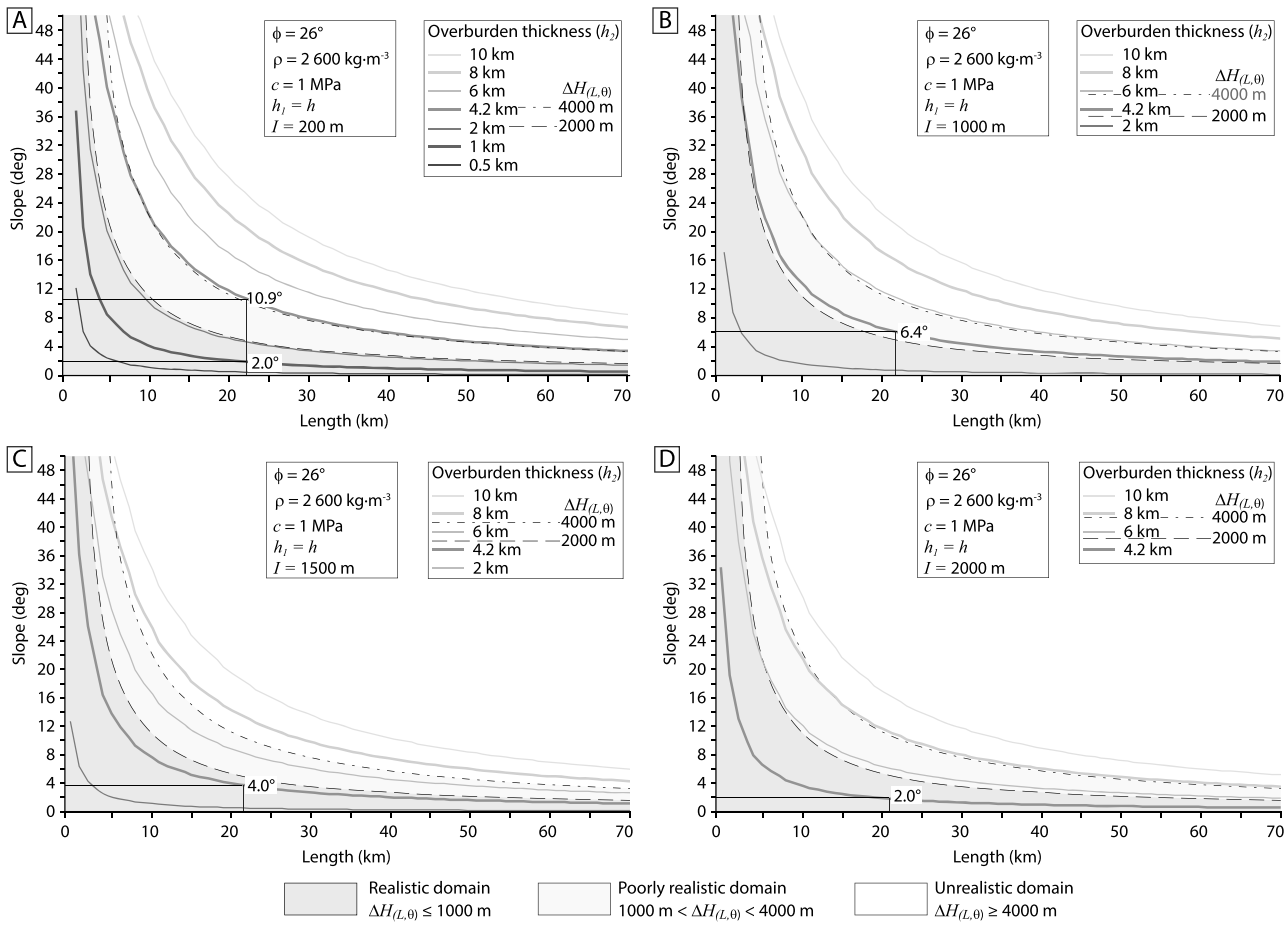

Figure 13. Results of the analytical model with incision: critical slope for sliding, as a function of the length of sliding sheet (L), for various values of overburden thickness (h) with incision depth (I) of (a) 200 m, (b) 1000 m, (c) 1500 m, and (d) 2000 m. $\Delta H_{(L,\theta)}$: difference in height as a function of the slope and the length.

initiation of gravity gliding on local to lithospheric scales. The dashed lines indicate a difference in elevation of 2000 and 4000 m corresponding to the slope versus length couple. Considering a constant dip of the basal detachment, we assume that the difference in height (ΔH; Figure 3) in continental environments rarely exceeds 2000 m and never 4000 m. Thus, we consider that gliding is unlikely when the ΔH value falls in the range 2000–4000 m, and unrealistic above 4000 m.

Figure 12a shows the analytical solutions obtained with a medium internal friction angle (ϕ =26°) and using the hydrostatic pore pressure set in the numerical models. The critical slope angle rapidly attains 30° for lengths shorter than 15 km and decreases to angles lower than 5° for 150 km long sliding sheets. Because the critical slope angle decreases with the thickness of the slide, irrespective of its length, gliding is always favored in the case of the thinnest overburden. Thus, as in the numerical models, the analytical critical slope angle would be higher for shorter lengths, with gravity gliding occurring first above the shallowest detachment. If we consider a 1 km thick overburden, the analytical solution yields critical slopes of 4.8° and 3.3° for slides with lengths of 15 km and 22 km that correspond, respectively, to the western and eastern limbs of the Chihuido North anticline. Similarly, the numerical *model 1* yields slope angles of 5.6° and 3.9°. These slightly higher values are probably due to the geometrical approximation of the analytical solution. According to the analytical solutions, the 4200 m thick overburden requires critical slopes of 17.5 and 12.1° above the short and long limbs, which are around 4 times higher than for a 1000 m deep décollement. These slopes are probably unrealistic in nature, since the difference in elevation (ΔH; Figure 3) would exceed 4000 m.

According to equation (12), the overburden will fail and move downslope when its weight (F_w) and the upslope force (F_u) exceed the downslope resistance (Fd). Considering that the overburden thickness is laterally

©2014. American Geophysical Union. All Rights Reserved.

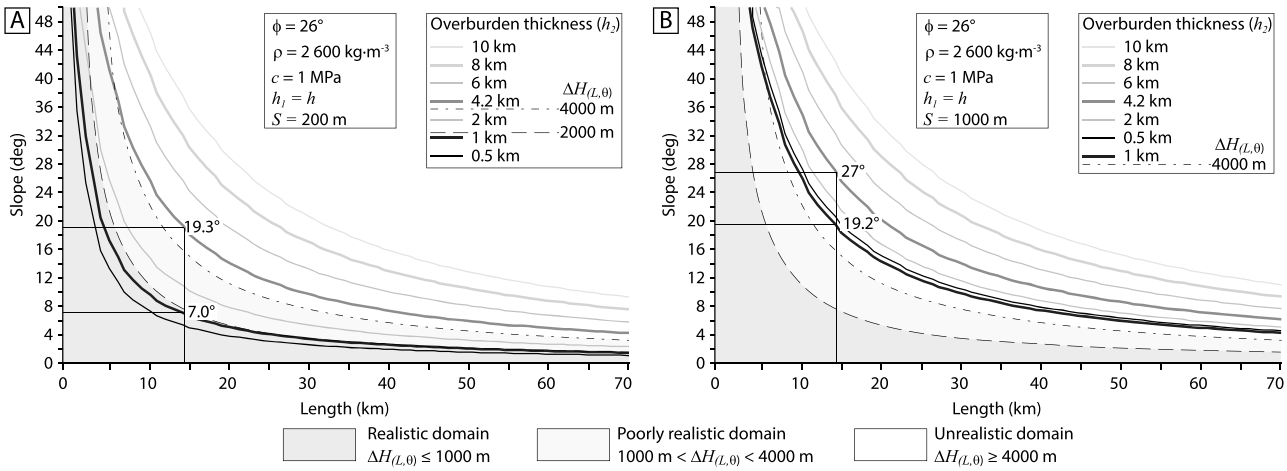

Figure 14. Results of the analytical model with sedimentation: critical slope for sliding, as a function of the length of sliding sheet (L), for various values of overburden thickness (h) with sedimentation thickness (S) of (a) 200 m and (b) 1000 m.
$\Delta H_{(L,\theta)}$: difference in height as a function of the slope and sheet length.

constant ($h_1 = h_2 = h$), the equation also holds true for the stress conditions ($\sigma = F/h$). Numerical and analytical results show that a 1000 m thick overburden would slide when σ_d, σ_u, and σ_w are equal to 36, 4, and 32 MPa, respectively, along both limbs. Because σ_w is not a function of the thickness, for similar lengths and slopes, its value remains the same for the 4200 m thick overburden. Nevertheless, in this case, σ_d and σ_u increase to 140 and 22 MPa. Hence, under these conditions, the weight is insufficient, and gravity gliding cannot occur above the deepest décollement layer in *model 1*. This demonstrates that contractional resistance at the toe of the slope is a primary factor controlling gliding dynamics, in accordance with previous studies [*Mourgues and Cobbold*, 2006; *Lacoste et al.*, 2012]. In addition, the analytical solutions show that gravity gliding in nature could occur when the décollement depth is shallower than 2000 m, while it is unlikely between 2000 and 4000 m, and certainly unrealistic at greater depths (Figure 12a).

5.3. Influence of Internal Friction Angle

According to *Chéry et al.* [2001], the friction angle needs to be adjusted to take account of pore pressure at the crustal scale. *Chéry et al.* [2001] simulated this rheological state using an effective friction angle (ϕ_{eff}) of 15–20° for a Drucker-Prager criterion. The Mohr-Coulomb criterion at yield point, assuming negligible cohesion, is given by $\sin(\phi) = (\sigma_1/\sigma_3 - 1)/(\sigma_1/\sigma_3 + 1)$. Since borehole measurements in regions with extensional and strike-slip stress regimes have shown that the σ_1/σ_3 ratio is always lower than 2 [*Brudy et al.*, 1997; *Zoback and Townend*, 2001], this leads us to obtain an effective friction angle lower than 19°. This result differs from laboratory experiments of *Byerlee* [1978] ($\phi \approx 30°$) and could be due to a scale effect, pore fluid pressure, and structural inheritance. For example, in the first steps of the uplift in our numerical models, extensional and compressional fracturing related to flexural bending may weaken the upper and lower hinges of the bulge, thus localizing the resistive domains of the gliding as discussed above.

Figures 12b–12d show the gliding conditions for several values of ϕ. For ϕ = 30°, according to *Byerlee* [1978], gravity gliding is unrealistic for thicknesses exceeding 2 km (Figure 12b). Gliding would be more probable for thicknesses of 3000–4000 m when associated with decreasing values of ϕ (Figures 12c and 12d). Considering the numerical *model 1*, gravity gliding remains likely above the shallower décollement whatever the value of ϕ, with critical slope angles ranging from 5.8 to 2.7° for the short limb and from 3.9 to 1.9° for the long limb (Figure 12). Gliding remains unrealistic for an overburden thickness of 4200 m whatever the value of ϕ.

5.4. Influence of Valley Incision and Deposition

$\vec{F}_d$ is affected by changes in the overburden thickness at the toe of the uplift (equation (5)). Removal of material will decrease the resistance to contractional failure, whereas deposition will increase the resistance. On the

©2014. American Geophysical Union. All Rights Reserved.

contrary, considering that the length and thickness of the translated raft are unchanged, $\vec{F}_w$ varies only with θ_c. Moreover, fluvial incision and/or sedimentation induce a pressure gradient in the overburden which induces Poiseuille flow $\vec{F}_p$ in the décollement layer. The presence of a valley generates a positive pressure gradient directed downslope, where $\vec{F}_p$ favors the formation of a slide. This gradient becomes negative in the case of deposition, and $\vec{F}_p$ resists the formation of a slide. To compare the analytical and numerical solutions, we set the thickness (h_s) of the shallow décollement layer at 200 m and at 300 m for deeper décollement. For these thicknesses, $\vec{F}_p$ decreases significantly the critical slope angle by about 1–10%, i.e., by ~1° when the overburden is short and thin, and by ~0.1° when the overburden is long and thick. Figure 13 shows the effect of depth of incision on the critical slope angle, assuming a valley of infinite width (with depths of 200 m, Figure 13a; 1000 m, Figure 13b; 1500 m, Figure 13c; and 2000 m, Figure 13d). The deepest valley is consistent with the amount of incision of the Colorado River (Utah, USA). A 200 m deep valley facilitates gravity gliding above décollements having depths inferior to 2000 m (Figure 13a). Gliding becomes possible above a 4200 m deep décollement in the case of an incision of 1000 to 1500 m (Figures 13b and 13c) and likely where incision reaches 2000 m (Figure 13d). Gravity gliding remains unlikely where décollements are deeper than 6000 m. The analytical solution yields a smaller critical slope (2.0°) along the long limb compared with the value of 3.9° obtained from *model 2* assuming a 200 m deep valley (Figure 13a). In that case, the analytical solution also suggests that gravity gliding cannot occur above a 4200 m deep décollement along the long limb. Indeed, the critical slope angle θ_c would have to reach 10.9°, while the slope is only 7.0° at the end of the numerical simulation (Figure 8).

Figure 14 shows analytical calculations of the influence of deposition at the toe of the uplifted zone. We tested the deposition thicknesses of 200 m (Figure 14a) and 1000 m (Figure 14b). In the former case, gravity gliding is inhibited above décollements located at depths superior than 1000 m (Figure 14a). According to the analytical solution, a slide along the short limb would be initiated at $\theta_c = 7.0°$ for a 15 km long overburden instead of at 8.8°, as indicated by the numerical *model 3*. The difference in elevation reaches around 2000 m, which explains why gravity gliding is negligible at the end of the numerical simulation. In addition, the analytical solution suggests that deposition having a thickness of more than 1000 m inhibits gravity gliding regardless of the depth to the detachment (Figure 14b). Note that the critical slope angle required to generate gliding becomes higher when the overburden thickness increases from 500 m to 1000 m, which is in contrast to the usual solutions. This probably reflects the resistance to gliding due to the effect of $\vec{F}_p$.

6. Discussion

Our numerical models are simplified prototypes designed to investigate the forcing factors that allow onland gravity gliding. Our models are not intended to simulate the details of geological processes operating in nature and are not expected to provide exact representations of the resulting structural styles. The models display plane strain cross sections with a geometrically simple sedimentary cover, as found in forelands, and are based on idealized material properties that are homogeneous along strike, without any preexisting relief. In nature, many other configurations of gravity gliding could be associated with other values of erosion, deposition, internal friction angle, viscosity, and thickness of the décollement layers.

In accordance with our results, numerical and analytical solutions and laboratory experiments have shown that dips lower than 5° are sufficient to generate large-scale gravity gliding as observed on passive margins [e.g., *Mandl and Crans*, 1981; *Vendeville et al*., 1987; *Rossello and Cobbold*, 1988; *Cobbold et al*., 1989; *Mauduit et al*., 1997a; *Duval et al*., 1992; *Lundin*, 1992; *Mourgues and Cobbold*., 2006; *Sellier et al*., 2013]. *Brun and Fort* [2011] proposed analytical solutions showing that dominant gravity gliding of overburdens up to 2000 m thick and several hundreds of kilometers long would occur on land for slope angles of 1° without abnormal fluid pressure in sediments or supplementary upslope load. Nevertheless, it remains unclear whether smaller-scale gliding could occur under such conditions.

The idea that smaller gravity-driven slides could occur on land has been investigated mechanically considering that river incision weakens the frontal buttress. For example, *McGill and Stromquist* [1979] interpreted a series of grabens in the Canyonlands National Park (Utah) as resulting from a gravity slide toward the canyon of the Colorado River. The rigid plate is 25 km long and 460 m thick and slides above a 300 to 450 m thick evaporite layer dipping at an angle of 1–2°. *Schultz-Ela and Walsh* [2002] presented a set of numerical models which

©2014. American Geophysical Union. All Rights Reserved.

simulate this gravity-driven slide without a frontal buttress. Assuming rheological properties similar to those used in our models, they concluded that sliding could be simulated for these conditions. *Lacoste et al.* [2009] questioned the link between gravity spreading and river incision. They investigated an example of river incision-related landslides in the Waitawhiti area (New Zealand) involving overburdens around 1 km long and 50 m thick with strata dipping nearly horizontal to 20°. Based on these settings, analogue experiments indicate that initial incision at the toe of the slope would trigger slides, especially when the process is continuous through time [*Lacoste et al.*, 2011, 2012]. Such configurations are consistent with our results (Figure 13). In addition, since river incision often attains the décollement layer, Poiseuille flow can play a significant role when this layer is composed of evaporites [*Schultz-Ela and Walsh*, 2002].

Using numerical models and the analytical solutions, we investigated the feasibility of onland gravity gliding in the Chihuidos area of the Andean fold belt (Figure 1). Results imply that a tilt of 3 to 5° in a 30 km long slab of sediments would be sufficient to generate gravitational instabilities in the uppermost kilometer (Figures 6 and 12). These conditions are encountered on the eastern limb of the Chihuido North anticline, suggesting that gravity gliding can occur. Solutions with a 200 m deep river valley at the toe of the long limb indicate that incision forms a weak zone which favors contractional failure and reduces the critical slope required for sliding by as much as 1° (Figures 8 and 13a). Thus, incision would facilitate gliding and lead to increased maturity of the extensional and contractional deformation. Such gliding could not occur above a 4200 m deep décollement layer (Figures 1, 6, and 12), which is consistent with the geological observations. Nevertheless, because the current structural slope of the short limb of the Chihuido North anticline exceeds the critical slope predicted by the numerical and analytical solutions, the short limb should have experienced deformation, even though *Messager et al.* [2014] failed to observe any evidence of this (Figures 1, 6, and 12a). However, geological observations argue for a 200 to 1000 m thick sedimentary thickening at the toe of this limb. For these values, our theoretical solutions show that deposition can inhibit gravity gliding (Figures 1, 10, and 14b). Thus, rather than the structural pattern of the Chihuidos Massif, Cretaceous to Neogene sedimentation and Quaternary river incision at the toes of the structure may have primarily controlled the onset of gravity gliding. On a more regional scale, Quaternary extension in the southern central Andes is mostly located above crustal-scale anticlines [e.g., *Narciso et al.*, 2000; *Folguera et al.*, 2008]. In a recent study, *Messager et al.* [2010] showed that some of these crustal structures were uplifted during the Quaternary, while fluvial incision of more than 1000 m took place in the Neuquén Basin during the Pleistocene, probably due to climatic forcing [*Rabassa and Clapperton*, 1990]. Thus, we can investigate the origin of some extensional structures in the light of criterion failure analysis of gravity-driven instabilities. In general, we infer that gravity gliding over distances of less than 100 km with an overburden thickness of up to 2000 m could be common in tectonically active foothills where incision is the rule.

Recent studies have suggested the possibility of such a process at the crustal scale. In the southwestern French Alps, *Rangin et al.* [2010] proposed that the 150 km long French Provençal Basin detached at a depth of 10 km above Triassic evaporites. Considering a density of 2800 kg m^{-3}, a cohesion of 1 MPa and a low internal friction angle of 15° [*Chéry et al.*, 2001], the critical slope exceeds the current average topographic gradient (0.95°; Figure 12d). For the critical slope to reach a value of 0.55°, the mechanical conditions require a thinning of around 2500–3000 m down the slope. Fluvial incision is insufficient to produce so much thinning; only oceanic basins can guide the location of a weak frontal buttress at the crustal scale as invoked by *Larroque et al.* [2009] in the southeastern French Alps. Nevertheless, these results suffer from some shortcomings due to the geometrical assumptions of the physical problem in 2-D, as well as uncertainties on the crustal rheology and the role of the spreading component.

7. Conclusions

Mechanisms allowing large-scale onland gravity gliding are investigated using 2-D finite element modeling and a 2-D analytical failure solution. Numerical models are used to simulate the shape of asymmetrical crustal-scale uplift near the Andean front. The sedimentary cover includes two thin décollement layers at depths of 1000 m and 4200 m. Uplift during the Quaternary is suspected to trigger the sliding of a 1000 m thick overburden above the long limb of the Chihuido North anticline. In this study, we examine the role of fluvial incision and sedimentation which occur at the toes of the structure. We consider that, unlike in passive margins or deltaic domains, upslope sedimentation and fluid overpressure in onland sediments are not driving forces.

©2014. American Geophysical Union. All Rights Reserved.

Finite deformation associated with the gravity gliding shows that the overburden slides only above the shallow décollement located at a depth of 1000 m. Extension is expressed by collapsed blocks on top of the uplift, while contraction is more diffuse at the toe of the limbs. Numerical and analytical results show that without incision and sedimentation, gliding occurs simultaneously above both limbs but is faster above the steeper short limb. Large-scale gravity gliding can be found in continental domains where overburden thickness is less than 2000 m; river incision reduces the critical slope angle and facilitates gliding above the long limb. Stretching is increased and shortening is concentrated in this weakened zone. River incision between 1000 and 2000 m deep may lead to overburden instabilities up to 4000 m thick; deposition increases the critical slope angle and gliding is negligible above the short limb. The deposition of sediments thicker than 1000 m would inhibit large-scale gravity gliding in nature.

In tectonically active regions, we show that uplift can generate slopes steep enough to initiate gravity instabilities and that incision reduces the downslope resistance to contractional failure, while sedimentation has the opposite effect. Our results show that gravity gliding is mechanically feasible in the case of the Chihuido North anticline. Considering both sediment storage and river incision, gravity gliding would occur only along the long limb, contrary to the prediction without incision or sedimentation. These results show that thin-skinned onland gravity gliding could be common in tectonically active regions where incision is the rule, which provides a potentially new explanation for the origin of thin-skinned extension in mountain ranges.

Acknowledgments
Our thanks to TOTAL DGEP/TDO/CA/AS/TEC (FR00002338), Jean-Paul Xavier and Yves Hervouët for funding and supporting our project in the Neuquén Basin. We deeply acknowledge Christopher Beaumont, Aurélien Lacoste, and Alexander Densmore for their constructive reviews. They substantially increased the impact of the manuscript. We thank Michael Carpenter who provided a smooth and correct English writing.

References

Berger, A., F. Jouanne, R. Hassani, and J. L. Mugnier (2004), Modelling the spatial distribution of present-day deformation in Nepal: How cylindrical is the main Himalayan thrust in Nepal?, *Geophys. J. Int.*, *156*, 94–114, doi:10.1111/j.1365-246X.2004.02038.x.

Bishop, D. J., P. G. Buchanan, and C. J. Bishop (1995), Gravity-driven thin-skinned extension above Zechstein Group evaporites in the western central North Sea: An application of computer-aided section restoration techniques, *Mar. Pet. Geol.*, *12*(2), 115–135, doi:10.1016/0264-8172(95)92834-J.

Bonnardot, M. A., R. Hassani, and E. Tric (2008), Numerical modelling of lithosphere-asthenosphere interaction in a subduction zone, *Earth Planet. Sci. Lett.*, *272*, 698–708, doi:10.1016/j.epsl.2008.06.009.

Brudy, M., M. D. Zoback, K. Fuchs, F. Rummel, and J. Baumgärtner (1997), Estimation of the complete stress tensor to 8 km depth in the KTB scientific drill holes: Implications for crustal strength, *J. Geophys. Res.*, *102*(B8), 18,453–18,475, doi:10.1029/96JB02942.

Brun, J.-P., and X. Fort (2011), Salt tectonics at passive margins: Geology versus models, *Mar. Pet. Geol.*, *28*(6), 1123–1145, doi:10.1016/j.marpetgeo.2011.03.004.

Burollet, P. F. (1975), Tectonique en radeaux en Angola, *Bull. Soc. Geol. Fr.*, *17*(4), 503–504, doi:10.2113/gssgfbull.S7-XVII.4.503.

Byerlee, J. (1978), Friction of rocks, *Pure Appl. Geophys.*, *116*(4-5), 615–626, doi:10.1007/BF00876528.

Chéry, J., M. D. Zoback, and R. Hassani (2001), An integrated mechanical model of the San Andreas fault in central and northern California, *J. Geophys. Res.*, *106*(B10), 22,051–22,066, doi:10.1029/2001JB000382.

Cobbold, P. R., and E. Rossello (2003), Aptian to recent compressional deformation, foothills of the Neuquén Basin, Argentina, *Mar. Pet. Geol.*, *20*(5), 429–443, doi:10.1016/S0264-8172(03)00077-1.

Cobbold, P. R., and P. Szatmari (1991), Radial gravitational gliding on passive margins, *Tectonophysics*, *188*(3–4), 249–289, doi:10.1016/0040-1951(91)90459-6.

Cobbold, P. R., E. Rossello, and B. Vendeville (1989), Some experiments on interacting sedimentation and deformation above salt horizons, *Bull. Soc. Geol. Fr.*, *5*(3), 453–460, doi:10.2113/gssgfbull.V.3.453.

Cobbold, P. R., R. Mourgues, and K. Boyd (2004), Mechanism of thin-skinned detachment in the Amazon fan: Assessing the importance of fluid overpressure and hydrocarbon generation, *Mar. Pet. Geol.*, *21*(8), 245–258, doi:10.1016/j.marpetgeo.2004.05.003.

Cobbold, P. R., B. J. Clarke, and H. Løseth (2009), Structural consequences of fluid overpressure and seepage forces in the outer thrust belt of the Niger Delta, *Pet. Geosci.*, *15*(1), 3–15, doi:10.1144/1354-079309-784.

Cohen, H. A., and K. McClay (1996), Sedimentation and shale tectonics of the northwestern Niger Delta front, *Mar. Pet. Geol.*, *13*(3), 313–328, doi:10.1016/0264-8172(95)00067-4.

Cundall, P., and M. Board (1988), A microcomputer program for modeling large strain plasticity problems, in *Numerical Methods in Geomechanics*, edited by C. Swoboda, pp. 2101–2108, Balkema, Rotterdam.

Dahlen, F. A. (1984), Noncohesive critical Coulomb wedges: An exact solution, *J. Geophys. Res.*, *89*(B12), 10,125–10,133, doi:10.1029/JB089iB12p10125.

Damuth, J. E. (1994), Neogene gravity tectonics and depositional processes on the deep Niger Delta continental margin, *Mar. Pet. Geol.*, *11*(3), 320–346, doi:10.1016/0264-8172(94)90053-1.

De Brodtkorb, M. K., V. Ramos, M. Barbieri, and S. Ametrano (1982), The evaporitic celestite-barite deposits of Neuquén, Argentina, *Miner. Deposita*, *17*(3), 423–436, doi:10.1007/BF00204470.

Demercian, S., P. Szatmari, and P. R. Cobbold (1993), Style and pattern of salt diapirs due to thin-skinned gravitational gliding, Campos and Santos Basins, *Tectonophysics*, *228*(3–4), 393–433, doi:10.1016/0040-1951(93)90351-J.

Duval, B., C. Cramez, and M. P. A. Jackson (1992), Raft tectonics in the Kwanza Basin, Angola, *Mar. Pet. Geol.*, *9*(4), 389–404, doi:10.1016/0264-8172(92)90050-O.

Einsele, G., and M. Hinderer (1997), Terrestrial sediment yield and the lifetimes of reservoirs, lakes, and larger basins, *Geol. Rundsch.*, *86*(2), 288–310, doi:10.1007/s005310050141.

Emami, H., J. Vergés, T. Nalpas, P. Gillespie, I. Sharp, R. Karpuz, E. P. Blanc, and M. G. H. Goodarzi (2010), Structure of the Mountain Front Flexure along the Anaran anticline in the Pusht-e Kuh Arc (NW Zagros, Iran): Insights from sand box models, *Geol. Soc. London Spec. Publ.*, *330*(1), 155–178, doi:10.1144/SP330.9.

©2014. American Geophysical Union. All Rights Reserved.

Evamy, B. D., J. Haremboure, P. Kamerling, W. A. Knaap, F. A. Molloy, and P. H. Rowlands (1978), Hydrocarbon habitat of Tertiary Niger Delta, *Am. Assoc. Pet. Geol. Bull.*, *62*(1), 1–32.

Folguera, A., G. Bottesi, V. A. Ramos, and T. Zapata (2008), Crustal collapse in the Andean backarc since 2 Ma: Tromen volcanic plateau, Southern Central Andes (36°40′–37°30′S), *Tectonophysics*, *459*(1), 140–160, doi:10.1016/j.tecto.2007.12.013.

Friedman, M., J. Handin, J. M. Logan, K. D. Min, and D. W. Stearns (1976), Experimental folding of rocks under confining pressure: Part III. Faulted drape folds in multilithologic layered specimens, *Geol. Soc. Am. Bull.*, *87*(7), 1049–1066, doi:10.1130/0016-7606(1976)87<1049:EFORUC>2.0.CO;2.

Galland, O., P. R. Cobbold, J. de Bremond d'Ars, and E. Hallot (2007), Rise and emplacement of magma during horizontal shortening of the brittle crust: Insights from experimental modeling, *J. Geophys. Res.*, *112*, B06402, doi:10.1029/2006JB004604.

Garcia-Castellanos, D. (2006), Long-term evolution of tectonic lakes: Climatic controls on the development of internally drained basins, in *Tectonics, Climate and Landscape Evolution*, *Spec. Pap.*, vol. 398, edited by S. D. Willett et al., pp. 283–294, Geol. Soc. Am., Boulder, Colo., doi:10.1130/2006.2398(17).

Gemmer, L., S. J. Ings, S. Medvedev, and C. Beaumont (2004), Salt tectonics driven by differential sediment loading: Stability analysis and finite element experiments, *Basin Res.*, *16*(2), 199–218, doi:10.1111/j.1365-2117.2004.00229.x.

Gemmer, L., C. Beaumont, and S. J. Ings (2005), Dynamic modelling of passive margin salt tectonics: Effects of water loading, sediment properties and sedimentation patterns, *Basin Res.*, *17*(3), 383–402, doi:10.1111/j.1365-2117.2005.00274.x.

Gerbault, M., J. Cembrano, C. Mpodozis, M. Farías, and M. Pardo (2009), Continental margin deformation along the Andean subduction zone: Thermomechanical models, *Phys. Earth Planet. Inter.*, *177*, 180–205, doi:10.1016/j.pepi.2009.09.001.

Giambiagi, L. B., M. Tunik, and M. Ghiglione (2001), Cenozoic tectonic evolution of the Alto Tunuyán foreland basin above the transition zone between the flat and normal subduction segment (33°30–34°S), western Argentina, *J. S. Am. Earth Sci.*, *14*(7), 707–724, doi:10.1016/S0895-9811(01)00059-1.

Got, J. L., V. Monteiller, J. Monteux, R. Hassani, and P. Okubo (2008), Deformation and rupture of the oceanic crust may control growth of Hawaiian volcanoes, *Nature*, *451*, 453–456, doi:10.1038/nature06481.

Gradmann, S., C. Beaumont, and M. Albertz (2009), Factors controlling the evolution of the Perdido Fold Belt, northwestern Gulf of Mexico, determined from numerical models, *Tectonics*, *28*, TC2002, doi:10.1029/2008TC002326.

Handin, J. (1966), Strength and ductility, in *Handbook of Physical Constants*, *Geol. Soc. Am. Mem.*, vol. 97, edited by S. P. Clark, pp. 223–290, The Geological Society of America, New York, doi:10.1130/MEM97-p223.

Hassani, R., D. Jongmans, and J. Chéry (1997), Study of plate deformation and stress in subduction processes using two-dimensional numerical models, *J. Geophys. Res.*, *102*(B8), 17,951–17,965, doi:10.1029/97JB01354.

Hilley, G. E., and M. R. Strecker (2005), Processes of oscillatory basin filling and excavation in a tectonically active orogen: Quebrada del Toro Basin, NW Argentina, *Geol. Soc. Am. Bull.*, *117*(7–8), 887–901, doi:10.1130/B25602.1.

Holmberg, E. (1964), Descripción geológica de la Hoja 33d, Auca Mahuida, Provincia del Neuquén, in *Boletín de la Dirección Nacional de Geología y Minería*, *Boletín*, vol. 94, pp. 1–88, República Argentina, Ministerio de Economía de la Nación, Secretaría de Industria y Minería, Subsecretaría de Minería, Dirección Nacional de Geología y Minería, Buenos Aires.

Holmberg, E. (1976), *Descripción Geológica de la Hoja 32c, Buta Ranquil, Provincia de Neuquén*, *Boletín*, vol. 152, pp. 1–90, Servicio Geológico Nacional, Buenos Aires.

Horton, B. K., and P. G. DeCelles (1997), The modern foreland basin system adjacent to the central Andes, *Geology*, *25*(10), 895–898, doi:10.1130/0091-7613(1997)025<0895:TMFBSA>2.3.CO;2.

Howell, J. A., E. Schwarz, L. A. Spalletti, and G. D. Veiga (2005), The Neuquén Basin: An overview, in *The Neuquén Basin: A Case Study in Sequence Stratigraphy and Basin Dynamics*, *Spec. Publ.*, vol. 252, edited by G. D. Veiga et al., pp. 1–14, Geological Society, London, doi:10.1144/GSL.SP.2005.252.01.01.

Hubbert, M. K., and W. W. Rubey (1959), Role of fluid pressure in mechanics of overthrust faulting I. Mechanics of fluid-filled porous solids and its application to overthrust faulting, *Geol. Soc. Am. Bull.*, *70*(2), 115–166, doi:10.1130/0016-7606(1959)70[115:ROFPIM]2.0.CO;2.

Huc, M., R. Hassani, and J. Chéry (1998), Large earthquake nucleation associated with stress exchange between middle and upper crust, *Geophys. Res. Lett.*, *25*(4), 551–554, doi:10.1029/98GL00091.

Humphrey, N. F., and S. K. Konrad (2000), River incision or diversion in response to bedrock uplift, *Geol. Soc. Am.*, *28*(1), 43–46, doi:10.1130/0091-7613(2000)28<43:RIODIR>2.0.CO;2.

Ibetsberger, H. J. (1996), The Tsergo Ri Landslide: An uncommon area of high morphological activity in the Langthang Valley, Nepal, *Tectonophysics*, *260*(1–3), 85–93, doi:10.1016/0040-1951(96)00077-7.

Jackson, J., R. Norris, and J. Youngson (1996), The structural evolution of active fault and fold systems in central Otago, New Zealand: Evidence revealed by drainage patterns, *J. Struct. Geol.*, *18*(2–3), 217–234, doi:10.1016/S0191-8141(96)80046-0.

Lacoste, A., L. Loncke, F. Chanier, J. Bailleul, B. C. Vendeville, and G. Mahieux (2009), Morphology and structure of a landslide complex in an active margin setting: The Waitawhiti complex, North Island, New Zealand, *Geomorphology*, *109*(3–4), 184–196, doi:10.1016/j.geomorph.2009.03.001.

Lacoste, A., B. C. Vendeville, and L. Loncke (2011), Influence of combined incision and fluid overpressure on slope stability: Experimental modelling and natural applications, *J. Struct. Geol.*, *33*(4), 731–742, doi:10.1016/j.jsg.2011.01.016.

Lacoste, A., B. C. Vendeville, R. Mourgues, L. Loncke, and M. Lebacq (2012), Gravitational instabilities triggered by fluid overpressure and downslope incision—Insights from analytical and analogue modelling, *J. Struct. Geol.*, *42*, 151–162, doi:10.1016/j.jsg.2012.05.011.

Larroque, C., B. Delouis, B. Godel, and J. M. Nocquet (2009), Active deformation at the southwestern Alps–Ligurian basin junction (France–Italy boundary): Evidence for recent change from compression to extension in the Argentera Massif, *Tectonophysics*, *467*(1–4), 22–34, doi:10.1016/j.tecto.2008.12.013.

Leanza, H. A., and C. A. Hugo (1999), Hoja Geológica 3969-I—Zapala, Provincia del Neuquén, in *Boletín Instituto de Geología y Recursos Naturales*, vol. 275, pp. 1–147, SEGEMAR, Buenos Aires.

Lesne, O., E. Calais, J. Deverchere, J. Chéry, and R. Hassani (2000), Dynamics of intracontinental extension in the north Baikal rift from two-dimensional numerical deformation modeling, *J. Geophys. Res.*, *105*(B9), 21,727–21,744, doi:10.1029/2000JB900139.

Lobkovsky, L. I., and V. I. Kerchman (1991), A two level concept of plate tectonics: Application to geodynamics, *Tectonophysics*, *199*(2–4), 343–374, doi:10.1016/0040-1951(91)90178-U.

Loncke, L., V. Gaullier, J. Mascle, B. Vendeville, and L. Camera (2006), The Nile deep-sea fan: An example of interacting sedimentation, salt tectonics, and inherited subsalt paleotopographic features, *Mar. Pet. Geol.*, *23*(3), 297–315, doi:10.1016/j.marpetgeo.2006.01.001.

Lundin, E. L. (1992), Thin-skinned extensional tectonics on a salt detachment, Northern Kwanza Basin, Angola, *Mar. Pet. Geol.*, *9*(4), 404–411, doi:10.1016/0264-8172(92)90051-F.

Lyons, W. A. (1980), Estudio Geológico–Minero de Las Salinas de Huitrín, Pcia del Neuquén, in *Informe final*, vol. 4643, Consejo Federal de Inversiones, pp. 1–173, Buenos Aires.

 ©2014. American Geophysical Union. All Rights Reserved.

Mandl, G., and W. Crans (1981), Gravitational gliding in deltas, in *Thrust and Nappes Tectonics*, edited by K. C. McClay and N. J. Price, *Geol. Soc. London Spec. Publ.*, *9*, 39–53, doi:10.1144/GSL.SP.1987.029.01.04.

Mauduit, T., and J. P. Brun (1998), Growth fault/rollover systems: Birth, growth, and decay, *J. Geophys. Res.*, *103*(B8), 18,119–18,136, doi:10.1029/97JB02484.

Mauduit, T., G. Guerin, J. P. Brun, and H. Lecanu (1997a), Raft tectonics: The effects of basal slope angle and sedimentation rate on progressive extension, *J. Struct. Geol.*, *19*(9), 1219–1230, doi:10.1016/S0191-8141(97)00037-0.

Mauduit, T., V. Gaullier, J. P. Brun, and G. Guerin (1997b), On the asymmetry of turtle-back growth anticlines, *Mar. Pet. Geol.*, *14*(7–8), 763–771, doi:10.1016/S0264-8172(97)00053-6.

McGill, G. E., and A. W. Stromquist (1979), The grabens of Canyonlands National Park, Utah: Geometry, mechanics, and kinematics, *J. Geophys. Res.*, *84*(B9), 4547–4563, doi:10.1029/JB084iB09p04547.

Mège, D., L. L. Deit, T. Rango, and T. Korme (2013), Gravity tectonics of topographic ridges: Halokinesis and gravitational spreading in the western Ogaden, Ethiopia, *Geomorphology*, *193*, 1–13, doi:10.1016/j.geomorph.2013.03.018.

Messager, G., B. Nivière, J. Martinod, P. Lacan, and J.-P. Xavier (2010), Geomorphic evidence for Plio-Quaternary compression in the southern Neuquén Basin, Argentina, *Tectonics*, *29*, TC4003, doi:10.1029/2009TC002609.

Messager, G., B. Nivière, P. Lacan, Y. Hervouët, and J.-P. Xavier (2014), Plio-Quaternary thin-skinned tectonics along the crustal front flexure of the southern central Andes: A record of the regional stress regime or of local tectonic-driven gravitational processes?, *Int. J. Earth Sci.*, *103*(3), 929–951, doi:10.1007/s00531-013-0983-4.

Mohriak, W. U., et al. (1995), Salt tectonics and structural styles in the deepwater province of the Cabo Frio region, Rio de Janeiro, Brazil, Salt tectonics: A global perspective, *AAPG Mem.*, *65*, 273–304.

Mosquera, A., and V. A. Ramos (2006), Intraplate deformation in the Neuquén Embayment, in *Evolution of an Andean Margin: A Tectonic and Magmatic View From the Andes to the Neuquén Basin (35°–39°S Lat)*, *Spec. Pap.*, vol. 407, edited by S. M. Kay and V. A. Ramos, pp. 97–123, Geol. Soc. Am.

Mourgues, R., and P. R. Cobbold (2003), Some tectonic consequences of fluid overpressures and seepage forces as demonstrated by sandbox modelling, *Tectonophysics*, *376*(1–2), 75–97, doi:10.1016/S0040-1951(03)00348-2.

Mourgues, R., and P. R. Cobbold (2006), Sandbox experiments on gravitational spreading and gliding in the presence of fluid overpressures, *J. Struct. Geol.*, *28*(5), 887–901, doi:10.1016/j.jsg.2005.12.013.

Mourgues, R., E. Lecomte, B. Vendeville, and S. Raillard (2009), An experimental investigation of gravity-driven shale tectonics in progradational delta, *Tectonophysics*, *474*(3), 643–656, doi:10.1016/j.tecto.2009.05.003.

Mourgues, R., A. Lacoste, and C. Garibaldi (2014), The Coulomb critical taper theory applied to gravitational instabilities, *J. Geophys. Res. Solid Earth*, *119*, 754–765, doi:10.1002/2013JB010359.

Narciso, V., G. R. Santamaría, and J. Zanettini (2000), Hoja geológica 3769-I: Barrancas, in *Boletín Instituto de Geología y Recursos Naturales*, *Boletín*, vol. 253, 60 pp., SEGEMAR, Buenos Aires.

Neves, S. P., A. Tommasi, A. Vauchez, and R. Hassani (2008), Intraplate continental deformation: Influence of a heat-producing layer in the lithospheric mantle, *Earth Planet. Sci. Lett.*, *274*(3–4), 392–400, doi:10.1016/j.epsl.2008.07.040.

Penge, J., B. Taylor, J. A. Huckerby, and J. W. Munns (1993), Extension and salt tectonics in the East Central Graben, in *Petroleum Geology of Northwestern Europe: Proceedings of the 4th Conference*, vol. 4, edited by J. R. Parker, pp. 1197–1210, Geological Society, London, doi:10.1144/0041197.

Philip, H., and J. F. Ritz (1999), Gigantic paleolandslide associated with active faulting along the Bogd fault (Gobi-Altay, Mongolia), *Geology*, *27*(3), 211–214, doi:10.1130/0091-7613(1999)027<0211:GPAWAF>2.3.CO;2.

Poliakov, A. N., and Y. Podladchikov (1992), Diapirism and topography, *Geophys. J. Int.*, *109*(3), 553–564, doi:10.1111/j.1365-246X.1992.tb00117.x.

Rabassa, J., and C. M. Clapperton (1990), Quaternary glaciations of the southern Andes, *Quat. Sci. Rev.*, *9*(2–3), 153–174, doi:10.1016/0277-3791(90)90016-4.

Ramos, V. A. (1981), *Descripción Geológica de la Hoja 33c, Los Chihuidos Norte, Provincia del Neuquén*, *Boletín*, vol. 182, pp. 1–103, Servicio Geológico Nacional, Buenos Aires.

Rangin, C., X. Le Pichon, Y. Hamon, N. Loget, and A. Crespy (2010), Gravity tectonics in the SE Basin (Provence, France) imaged from seismic reflection data, *Bull. Soc. Geol. Fr.*, *181*(6), 503–530, doi:10.2113/gssgfbull.181.6.503.

Rossello, E. A., and P. R. Cobbold (1988), Glissements gravitaires synsédimentaires sur marge continentale passive: Modéles analogiques, *Tech. Rep.*, Convention CFP/Université de Rennes.

Rowan, M. G., B. D. Trudgill, and J. C. Fiduk (2000), Deep-water, salt-cored foldbelts: Lessons from the Mississippi Fan and Perdido-fold-belts, northern Gulf of Mexico, in *Atlantic Rifts and Continental Margins*, *Geophys. Monogr. Ser.*, vol. 115, edited by W. U. Mohriak and M. Talwani, pp. 173–191, AGU, Washington, D. C., doi:10.1029/GM115p0173.

Schultz-Ela, D. D. (2001), Excursus on gravity gliding and gravity spreading, *J. Struct. Geol.*, *23*(5), 725–731, doi:10.1016/S0191-8141(01)00004-9.

Schultz-Ela, D. D., and P. Walsh (2002), Modeling of grabens extending above evaporites in Canyonlands National Park, Utah, *J. Struct. Geol.*, *24*(2), 247–275, doi:10.1016/S0191-8141(01)00066-9.

Sellier, N. C., L. Loncke, B. C. Vendeville, J. Mascle, T. Zitter, J. Woodside, and B. Loubrieu (2013), Post-Messinian evolution of the Florence Ridge area (Western Cyprus Arc). Part I: Morphostructural analysis, *Tectonophysics*, *591*, 131–142, doi:10.1016/j.tecto.2012.04.001.

Sobel, E. R., G. E. Hilley, and M. R. Strecker (2003), Formation of internally drained contractional basins by aridity-limited bedrock incision, *J. Geophys. Res.*, *108*(B7), 2344, doi:10.1029/2002JB001883.

Suppe, J., G. T. Chou, and S. C. Hook (1992), Rates of folding and faulting determined from growth strata, in *Thrust Tectonics*, edited by K. R. McClay, pp. 105–122, Chapman and Hall, London, doi:10.1007/978-94-011-3066-0_9.

Szatmari, P., M. C. M. Guerra, and M. A. Pequeno (1996), Genesis of large counter regional fault by flow of Cretaceous salt in the South Atlantic Santos Basin, Brazil, in *Salt Tectonics*, *Spec. Publ.*, vol. 100, edited by D. J. Blundel, G. I. Alsop, and J. Davison, pp. 259–264, Geological Society, London, doi:10.1144/GSL.SP.1996.100.01.16.

Tezón, R., et al. (1969), South America, in *Handbook of World Salt Resources*, *Monogr. Geosci.*, pp. 150–171, Springer, doi:10.1007/978-1-4684-0703-7_4.

Turcotte, D. L., and G. Schubert (1982), *Geodynamics: Applications of Continuum Physics to Geological Problems*, 450 pp., John Wiley, New York.

Underwood, P. (1983), Dynamic relaxation, in *Computational Methods for Transient Analysis (A 84-29160 12-64)*, edited by T. Belytschko and T. Hughes, pp. 245–265, Elsevier Science, Amsterdam, North-Holland.

van Keken, P. E., C. J. Spiers, A. P. van den Berg, and E. J. Muyzert (1993), The effective viscosity of rocksalt: Implementation of steady-state creep laws in numerical models of salt diapirism, *Tectonophysics*, *225*(4), 457–476, doi:10.1016/0040-1951(93)90310-G.

Vanbrabant, Y., D. Jongmans, R. Hassani, and D. Bellino (1997), An application of two-dimensional finite-element modelling for studying the deformation of the Variscan fold-and-thrust belt (Belgium), *Tectonophysics*, *309*(1–4), 141–159, doi:10.1016/S0040-1951(99)00136-5.

Vendeville, B., P. R. Cobbold, P. Davy, J. P. Brun, and P. Choukroune (1987), Physical models of extensional tectonics at various scales, in *Continental Extensional Tectonics*, *Spec. Publ.*, vol. 28, edited by J. F. Dewey and P. L. Hancock, pp. 95–107, Geological Society, London, doi:10.1144/GSL.SP.1987.028.01.08.

©2014. American Geophysical Union. All Rights Reserved.

Worral, D. M., and S. Snelson (1989), Evolution of the northern Gulf of Mexico, with emphasis on Cenozoic growth faulting and the role of salt, in *The Geology of North America: An Overview*, *Decade North Am. Geol.*, vol. A, edited by A. W. Bally and A. R. Palmer, pp. 97–138, Geol. Soc. of Am., Boulder, Colo.

Wu, S., A. W. Bally, and C. Cramez (1990), Allochthonous salt, structure and stratigraphy of the north-eastern Gulf of Mexico. Part II: Structure, *Mar. Pet. Geol.*, *7*(4), 334–370, doi:10.1016/0264-8172(90)90014-8.

Xiao, H.-B., F. A. Dahlen, and J. Suppe (1991), Mechanics of extensional wedges, *J. Geophys. Res.*, *96*(B6), 10,301–10,318, doi:10.1029/91JB00222.

Zapata, T. R., G. Zamora, and A. Ansa (2003), The Agrio fold and thrust belt: Structural analysis and its relationship with the petroleum system Vaca Muerta-Agrio-Troncoso inferior, *Exploration Petrolera en las Cuencas Subandinas, VIII Simposio Bolivariano*, vol. 1, pp. 168–176, VIII Simposio Bolivariano Tomo, Argentina.

Zoback, M. D., and J. Townend (2001), Implications of hydrostatic pore pressures and high crustal strength for the deformation of intraplate lithosphere, *Tectonophysics*, *336*, 19–30, doi:10.1016/S0040-1951(01)00091-9.

Zöllner, W., and A. J. Amos (1973), Descripción geológica de la Hoja 32b, Chos Malal, Provincia del Neuquén, in *Servicio Geológico Minero Argentino*, *Boletín*, vol. 143, pp. 1–91, Subsecretaría de Mineria, Buenos Aires.

©2014. American Geophysical Union. All Rights Reserved.